Subcontractor Report

High-Efficiency Triple-Junction Amorphous Silicon Alloy Photovoltaic Technology

Annual Technical Progress Report
6 March 1998 — 5 March 1999

S. Guha
United Solar Systems Corp.
Troy, Michigan

NREL

National Renewable Energy Laboratory

High-Efficiency Triple-Junction Amorphous Silicon Alloy Photovoltaic Technology

Annual Technical Progress Report
6 March 1998 — 5 March 1999

S. Guha
United Solar Systems Corp.
Troy, Michigan

NREL

National Renewable Energy Laboratory

NOTICE

This report was prepared as an account of work sponsored by an agency of the United States government. Neither the United States government nor any agency thereof, nor any of their employees, makes any warranty, express or implied, or assumes any legal liability or responsibility for the accuracy, completeness, or usefulness of any information, apparatus, product, or process disclosed, or represents that its use would not infringe privately owned rights. Reference herein to any specific commercial product, process, or service by trade name, trademark, manufacturer, or otherwise does not necessarily constitute or imply its endorsement, recommendation, or favoring by the United States government or any agency thereof. The views and opinions of authors expressed herein do not necessarily state or reflect those of the United States government or any agency thereof.

Available to DOE and DOE contractors from:
Office of Scientific and Technical Information (OSTI)
P.O. Box 62
Oak Ridge, TN 37831
Prices available by calling 423-576-8401

Available to the public from:
National Technical Information Service (NTIS)
U.S. Department of Commerce
5285 Port Royal Road
Springfield, VA 22161
703-605-6000 or 800-553-6847
or
DOE Information Bridge
http://www.doe.gov/bridge/home.html

Printed on paper containing at least 50% wastepaper, including 20% postconsumer waste

Preface

This Annual Subcontract Report covers the work performed by United Solar Systems Corp. for the period March 6, 1998 to March 5, 1999 under DOE/NREL Subcontract No. ZAK-8-17619-09. The following personnel participated in the research program.

A. Banerjee, E. Chen, J. Edens, T. Glatfelter, S. Guha (Principal Investigator), G. Hammond, M. Hopson, N. Jackett, K. Lord, A. Mohsin, J. Noch, T. Palmer, D. Wolf, B. Yan, J. Yang, and K. Younan.

Collaboration with the Colorado School of Mines, University of Oregon, National Renewable Energy Laboratory, and Energy Conversion Devices, Inc. is acknowledged. We would like to thank V. Trudeau for preparation of this report.

Table of Contents

iii

List of Figures

List of Tables

Executive Summary

Objectives

The principal objective of this R&D program is to expand, enhance and accelerate knowledge and capabilities for the development of high-performance, two-terminal multijunction hydrogenated amorphous silicon alloy cells and modules with low manufacturing cost and high reliability. The program goal is to obtain 12% stable modules that will qualify IEEE-Std 1262-1995 reliability testing.

Approach

In order to improve efficiency, United Solar uses a spectral-splitting, triple-junction cell structure. In this configuration, the top cell uses an amorphous silicon alloy of ~1.8 eV bandgap to absorb the blue photons. The middle cell uses an amorphous silicon germanium alloy (~20% germanium) of ~1.6 eV bandgap to capture the green photons. The bottom cell has ~40% germanium to reduce the bandgap to ~1.4 eV to capture the red photons. The cells are deposited on stainless steel with a predeposited silver/zinc oxide back reflector to facilitate light trapping. A thin layer of antireflection coating is applied to the top of the cell to reduce reflection loss.

During this year, research activities were carried out in the following four areas: 1) fundamental studies to improve our understanding of materials and devices, 2) small-area cell research to obtain the highest cell efficiency, 3) deposition of small-area cells using a modified very high frequency (MVHF) technique to obtain higher deposition rates, and 4) large-area cell research to obtain the highest module efficiency.

Status/Accomplishments

1.   Fundamental Studies

We have shown previously that hydrogen dilution plays a very important role in improving material and cell performance. The highest efficiency cells are obtained when the intrinsic material is deposited at a level of hydrogen dilution that is at the threshold between amorphous and microcrystalline transition. Collaborating with the Colorado School of Mines, we have now demonstrated that the structural order in this material is determined by the substrate on which the film is grown and also the film thickness. The order improves as the thickness increases. This results in the improvement of material quality in the direction of film growth and has been confirmed by the measurement of defect density at the University of Oregon.

2.   Small-area Cell Research

We have worked on improving the component cells of the multijunction structure by changing the deposition conditions. The highest efficiencies obtained in the multijunction structure are given below.

- Achieved 14.4% initial and 12.4% stable active-area (~0.25 cm^2) cell efficiency in a dual-bandgap, double-junction structure.

- Achieved 15.2% initial active-area (~0.25 cm^2) cell efficiency in a triple-junction structure.

3.   Cells Deposited at High Rates

We have previously shown that deposition at high rates results in poorer cell performance and stability. This was attributed to a poor microstructure of the film growth at high rates. Since the characteristic of the plasma can influence the film property significantly, we have carried out experiments to determine the energy distribution of the ionized species in the plasma excited by both radio frequency and very high frequency power sources. The energy of the positive ions is found to increase as the pressure is lowered. The following results have been obtained by using deposition rates of ~3-5 Å /s:

- Deposited single-junction top cells (~0.25 cm^2) on stainless steel substrates without back reflector using a-Si alloy at 3-5 Å /s and achieved a total-area stabilized cell efficiency of 4.85% measured under global AM1.5 after 1000 hours of one-sun light soaking at 50 ^{o}C.

- Deposited single-junction middle cells (~0.25 cm^2) on stainless steel substrates without back reflector using a-SiGe alloy at 3-5 Å /s and achieved a total-area stabilized power output of 2.73 mW/cm^2 measured under global AM1.5 with a λ>530 nm filter after 1240 hours of one-sun light soaking with an appropriate filter at 50 ^{o}C.

- Deposited single-junction bottom cells (~0.25 cm^2) on optimized back reflector using a-SiGe alloy at 3-5 Å /s and achieved a total-area stabilized power output of 3.11 mW/cm^2 measured under global AM1.5 with a λ>630 nm filter after 1043 hours of one-sun light soaking with an appropriate filter at 50 ^{o}C.

4.   Large-area Module Research

Uniformity in deposition over a large area is key to the achievement of high module efficiency. We use a large-area reactor where the component cells are deposited over one-square-foot area and the uniformity is investigated by evaluating the performance of small-area cells deposited over the entire area. Using this method, we have made high efficiency component cells and have fabricated large-area, triple-junction modules. The highlights of this activity are given below:

- Deposited array of single-junction top cells (~0.268 cm^2) on stainless steel substrates without back reflector using a-Si alloy over areas greater than 900 cm^2 and achieved an average total-area stabilized cell efficiency measured under global AM1.5 of 5.4% after 1031 hours of one-sun light soaking at 50 ^{o}C.

- Deposited array of single-junction middle cells (~0.268 cm^2) on stainless steel substrates without back reflector using a-SiGe alloy over areas greater than 900 cm^2 and achieved an average total-area stabilized power output measured under global AM1.5 with λ>530 nm filter of 3.6 mW/cm^2 after 1072 hours of one-sun light soaking with an appropriate filter at 50 ^{o}C.

- Deposited array of single-junction bottom cells (~0.268 cm^2) on optimized back reflector substrates using a-SiGe alloy over areas greater than 900 cm^2 and achieved an average total-area stabilized power output measured under global AM1.5 with λ>630 nm filter of 3.17 mW/cm^2 after 621 hours of one-sun light soaking with an appropriate filter at 50 ^{o}C.

- Deposited array of triple-junction cells (~0.268 cm^2) on optimized back reflector substrates using optimized component cells over areas greater than 900 cm^2 and achieved an average total-area stabilized efficiency measured under global AM1.5 of 11.6% after 1067 hours of one-sun light soaking at 50 ^{o}C.

- Achieved 10.5% stable aperture-area (~905 cm^2) efficiency in an encapsulated triple-junction

module after 1000 hours of one-sun light soaking at 50 °C carried out and measured by NREL.

- Fabricated and delivered two large-area prototype modules with a total area of 216" x 29.6" and 216" x 15.5" to NREL; the initial power outputs for the two modules are 317.8 W and 155.5 W, respectively, measured at NREL.

Major Publications

1. Guha, S.; Yang, J.; Banerjee, A.; Sugiyama, S. (1998). "Material issues in the commercialization of amorphous silicon alloy thin-film photovoltaic technology." *Mater. Res. Soc. Symp. Proc.*; Vol. 507, p. 99.

2. Yang, J.; Sugiyama, S.; Guha, S. (1998). "Effect of excitation frequency on the performance of amorphous silicon alloy solar cells." *Mater. Res. Soc. Symp. Proc.*; Vol. 507, p. 157.

3. Chen, C.C.; Lubianiker, Y.; Cohen, J.D.; Yang, J.; Guha, S.; Wickboldt, P.; Paul, W. (1998). "The electronic structure, metastability and transport properties of optimized amorphous silicon-germanium alloys." *Mater. Res. Soc. Symp. Proc.*; Vol. 507, p. 769.

4. Mahan, A.H.; Reedy, R.C., Jr.; Iwaniczko, E.; Wang, Q.; Nelson, B.P.; Xu, Y.; Gallagher, A.C.; Branz, H.M.; Crandall, R.S.; Yang, J.; Guha, S. (1998). "H out-diffusion and device performance in *n-i-p* solar cells utilizing high temperature hot wire a-Si:H i-layers." *Mater. Res. Soc. Symp. Proc.*; Vol. 507, p. 119.

5. Jiang, L.; Schiff, E.; Wang, Q.; Guha, S.; Yang, J. (1998). "Grazing incidence measurements of polarized electroabsorption and light soaking effect on amorphous silicon based solar cells." *Mater. Res. Soc. Symp. Proc.*; Vol. 507, p. 631.

6. Yang, J.; Banerjee, A.; Lord, K.; Guha, S. (1998). "Correlation of component cells with high efficiency amorphous silicon alloy triple-junction solar cells and modules." *2nd World Conference and Exhibition on Photovoltaic Solar Energy Conversion Proceedings;* p. 387.

7. Guha, S.; Yang, J.; Banerjee, A.; Hoffman, K.; Call, J. (1998). "Manufacturing issues for large volume production of amorphous silicon alloy photovoltaic modules." *NCPV Photovoltaics Program Review Proceedings;* p. 88.

8. Jiang, L.; Wang, Q.; Schiff, E.; Guha, S.; Yang, J. (1998). "Polarized electroabsorption spectra and light soaking of solar cells based on hydrogenated amorphous silicon." *Appl. Phys. Lett.*; Vol. 72, p. 1060.

9. Chen, C.; Zhong, F.; Cohen, J.D.; Yang, J.; Guha, S. (1998). "Evidence for charged defects in intrinsic glow-discharge hydrogenated amorphous silicon-germanium alloys." *Phys Rev. B*; Vol. 57 Rapid Communications, p. 4210.

10. Guha, S.; Yang, J.; Williamson, D.L.; Lubianiker, Y.; Cohen, J.D.; Mahan, A.H. (1999). "Structural, defect, and device behavior of hydrogenated amorphous Si near and above the onset of microcrystallinity." *Appl. Phys. Lett.*; Vol. 74, p. 1860.

Section 1

Introduction

This report describes the research performed during Phase I of a three-phase, three-year program under NREL Subcontract No. ZAK-8-17619-09. The research program is intended to expand, enhance and accelerate knowledge and capabilities for the development of high-performance, two-terminal multijunction amorphous silicon (a-Si) alloy cells and modules with low manufacturing cost and high reliability.

In order to improve efficiency, United Solar uses a spectral-splitting, triple-junction cell structure. In this configuration, the top cell uses an amorphous silicon alloy of ~1.8 eV bandgap to absorb the blue photons. The middle cell uses an amorphous silicon germanium alloy (~20% germanium) of ~1.6 eV bandgap to capture the green photons. The bottom cell has ~40% germanium to reduce the bandgap to ~1.4 eV to capture the red photons. The cells are deposited on stainless steel with a predeposited silver/zinc oxide back reflector to facilitate light trapping. A thin layer of antireflection coating is applied to the top of the cell to reduce reflection loss.

During this year, research activities were carried out in the following four areas: 1) fundamental studies to improve our understanding of materials and devices, 2) small-area cell research to obtain the highest cell efficiency, 3) deposition of small-area cells using a modified very high frequency (MVHF) technique to obtain higher deposition rates, and 4) large-area cell research to obtain the highest module efficiency. Results on 1) and 2) are described in Section 2. Data on higher deposition rates are given in Section 3. Module research activities are detailed in Section 4. Section 5 gives future directions.

Section 2

Amorphous Silicon Alloy Materials and Solar Cells Near the Threshold of Microcrystallinity

Introduction

Over the last two decades, photovoltaic (PV) technology using amorphous silicon (a-Si) alloy materials has advanced significantly to a stage where large-scale manufacturing is taking place worldwide (Rannels 1998). Most of the products to date are aimed at terrestrial applications such as battery charging and building-integrated photovoltaics. On the other hand, due to the tremendous growth in the field of telecommunication, intensive efforts are underway to qualify the lightweight inexpensive thin-film solar cells for space applications (Guha et al. 1998). Today, state-of-the-art a-Si alloy triple-junction modules on thin, flexible substrates are being seriously evaluated in orbit such as those from United Solar Systems Corp. (United Solar) on board the MIR space station.

Despite the substantial progress made in recent years, the biggest challenge for both terrestrial and extraterrestrial applications today is achieving even higher conversion efficiencies. A National Thin-film Partnership Team including members from the PV industry, universities, and national laboratories was organized in 1992 by the National Renewable Energy Laboratory (NREL) to coordinate and address various aspects of the thin-film materials and devices (von Roedern et al. 1997). A broad spectrum of activities, ranging from fundamental material studies to novel multijunction designs, has been addressed. In the last several years, the most important finding from these activities for improving stabilized cell efficiencies using plasma-enhanced chemical vapor deposition (PECVD) is probably the realization of the benefit of using hydrogen dilution during film growth (Yang et al. 1994). Although the first report on the effect of hydrogen dilution was made in 1981 by Guha et al. (Guha et al. 1981), it was not until the 1990's that improvement on solar cell performance using this approach became available in the literature. These cells exhibit higher efficiencies and better light stability.

A recent study by Tsu et al. (Tsu et al. 1997) further revealed that a-Si alloy materials grown using appropriate hydrogen dilution result in more-ordered microstructures in that intermediate-range orders have been observed. As the hydrogen dilution ratio is increased, there exists a transitional region beyond which microcrystallites begin to form rapidly. The best quality a-Si alloy solar cells are obtained when one deposits the material just below the threshold of the amorphous to microcrystalline transition. In this section, we review some interesting features associated with the materials near the threshold and discuss the corresponding solar cell performance.

Experimental Results and Discussion

Near Threshold Material Characteristics

The first experimental observation of improved stability against light soaking by using hydrogen dilution during film growth was reported by Guha at al. in 1981 (Guha et al. 1981). They found that films obtained using 10% silane (SiH_4) and 90% hydrogen (H_2) exhibited better stability than those grown using 100% SiH_4.

In 1994, we reported that a-Si alloy solar cells whose intrinsic layers were made with high hydrogen dilution displayed better stability than those made with low dilution at a same deposition temperature of 300 ^{o}C (Yang et al. 1994). In order to understand the difference in the two types of materials, we measured film properties such as infrared (IR) absorption, optical bandgap, hydrogen evolution, and small-angle X-ray scattering (SAXS). From the IR absorption spectra and optical bandgap measurements, we found that both types of materials contain ~10% of bonded hydrogen, and their optical bandgaps around 1.72 eV are also similar. On the other hand, the hydrogen evolution spectra for the two types of materials are distinctly different, as shown in Fig. 1. The low dilution sample exhibited a broad evolution peak near 500 ^{o}C (Fig. 1(a)), while the high dilution sample displayed a sharp, narrow peak near 400 ^{o}C (Fig. 1(b)) (Xu et al. 1996). This pronounced difference suggests that the microstructure of the two types of films may be quite different. Based on the IR analyses, it was pointed out that the low temperature evolution peak was not associated with dihydride or polyhydride structures. In addition, SAXS data showed that high hydrogen dilution samples contain oriented microstructures parallel to the film growth direction (Jones et al. 1993, Williamson 1995). Based on hydrogen evolution and SAXS data, it appears that the high dilution samples may have a heterogeneous structure.

Furthermore, we have made a-Si alloy solar cells using a gas mixture of SiD_4 and D_2 and compared the cell performance to those obtained from SiH_4 and H_2. We found that, using similar deposition conditions and intrinsic layer thicknesses, the deuterated cells show better stability against light soaking than the hydrogenated counterparts (Sugiyama et al. 1997). What is also interesting is that the deuterium evolution spectrum also showed a sharp, low temperature peak near 400 ^{o}C, displayed in Fig. 2.

From the above experimental results, it appears that the deposition conditions used for achieving more stable solar cells also lead to materials having a low temperature peak in the evolution spectra. A better stability seems to be correlated with an improved microstructure.

In order to further investigate the correlation between enhanced stability and the effect of hydrogen dilution, we collaborated with Tsu et al. (Tsu et al. 1997) and carried out a systematic study on samples prepared with low, medium, and high hydrogen dilutions. We used high resolution transmission electron microscopy (TEM) and Raman scattering measurements to look for qualitative and quantitative differences in the three types of films. Figure 3 shows the Raman spectra for a-Si alloy films of ~500 Å thick deposited on 7059 Corning glass. The low, medium, and high dilution films are shown in Fig. 3(b), 3(c), and 3(d), respectively. Also shown in Fig. 3(a) is a standard a-Si alloy film prepared with no hydrogen dilution. The following two observations are made. First of all, there is a shift in the Si TO peak position, indicated by the dashed line, from no dilution to high dilution. Secondly, a sharp band appeared at 516.5 cm^{-1} for the high dilution sample (Fig. 3(d)), and is attributed to microcrystalline inclusions. From this study, a clear trend emerges in that as the hydrogen dilution increases, it promotes the formation of microcrystallites in the amorphous matrix.

The films were subsequently lifted off the 7059 glass substrates and their microstructures analyzed by TEM. For the high dilution sample, distinct microcrystallites were indeed observed embedded in the featureless amorphous matrix even under low magnification. These spherical microcrystallites have sizes ranging from 2 to 10 nm in diameter. Under high magnification, TEM micrograph revealed that the high dilution sample exhibited long parallel lines separated by 0.31 nm, corresponding to the d spacing of Si (111) planes. In addition, one-dimensional linear-like objects that appear to have some degree of order along the length were observed. These objects have widths of 2-3 nm and lengths of up to a few 10's of nm. In fact, a careful examination of the other three samples showed that they all contain, to a lesser degree, these linear-like objects. This is true even for the standard sample prepared with no hydrogen dilution. Based on TEM and Raman data, we conclude that the intermediate range order of different
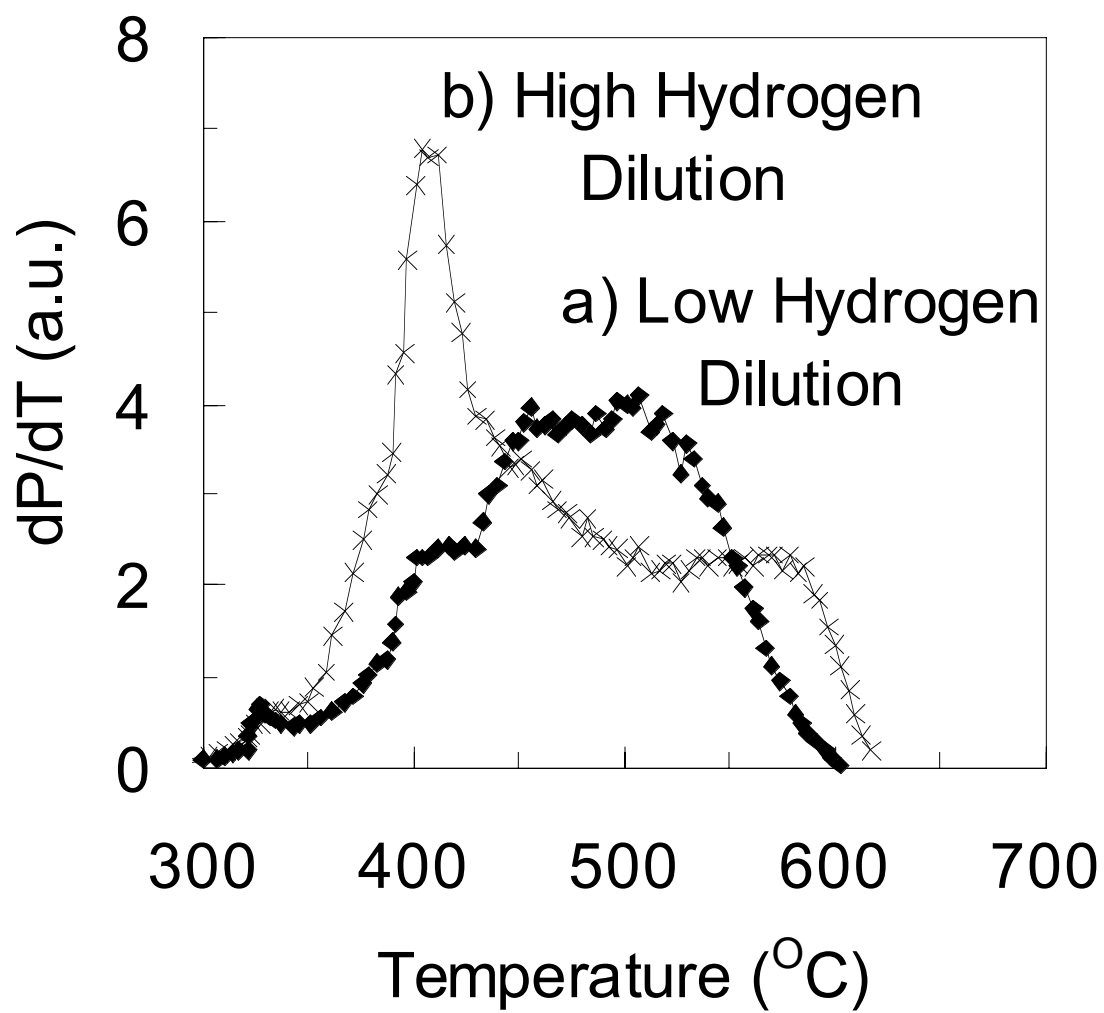
Figure 1. Hydrogen evolution spectra for (a) the low dilution and (b) the high dilution samples.
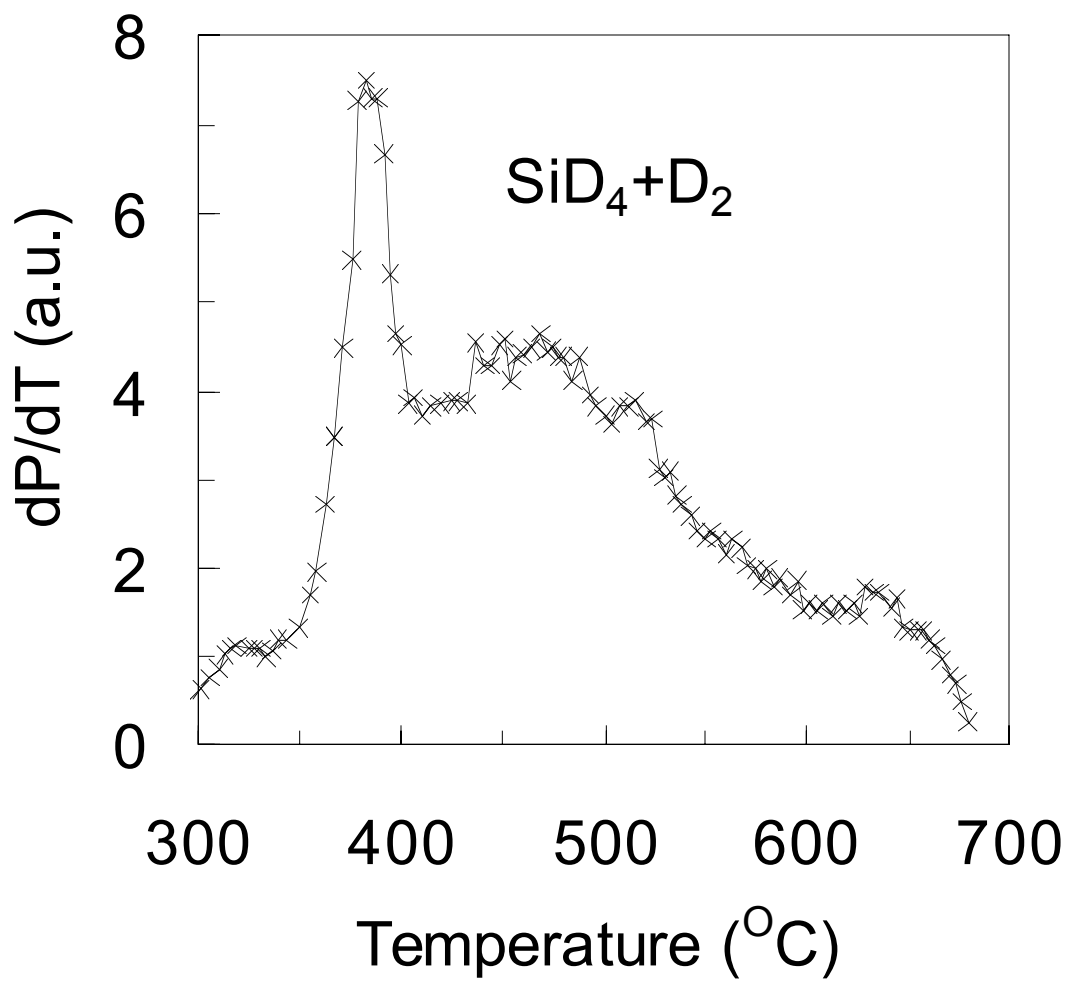
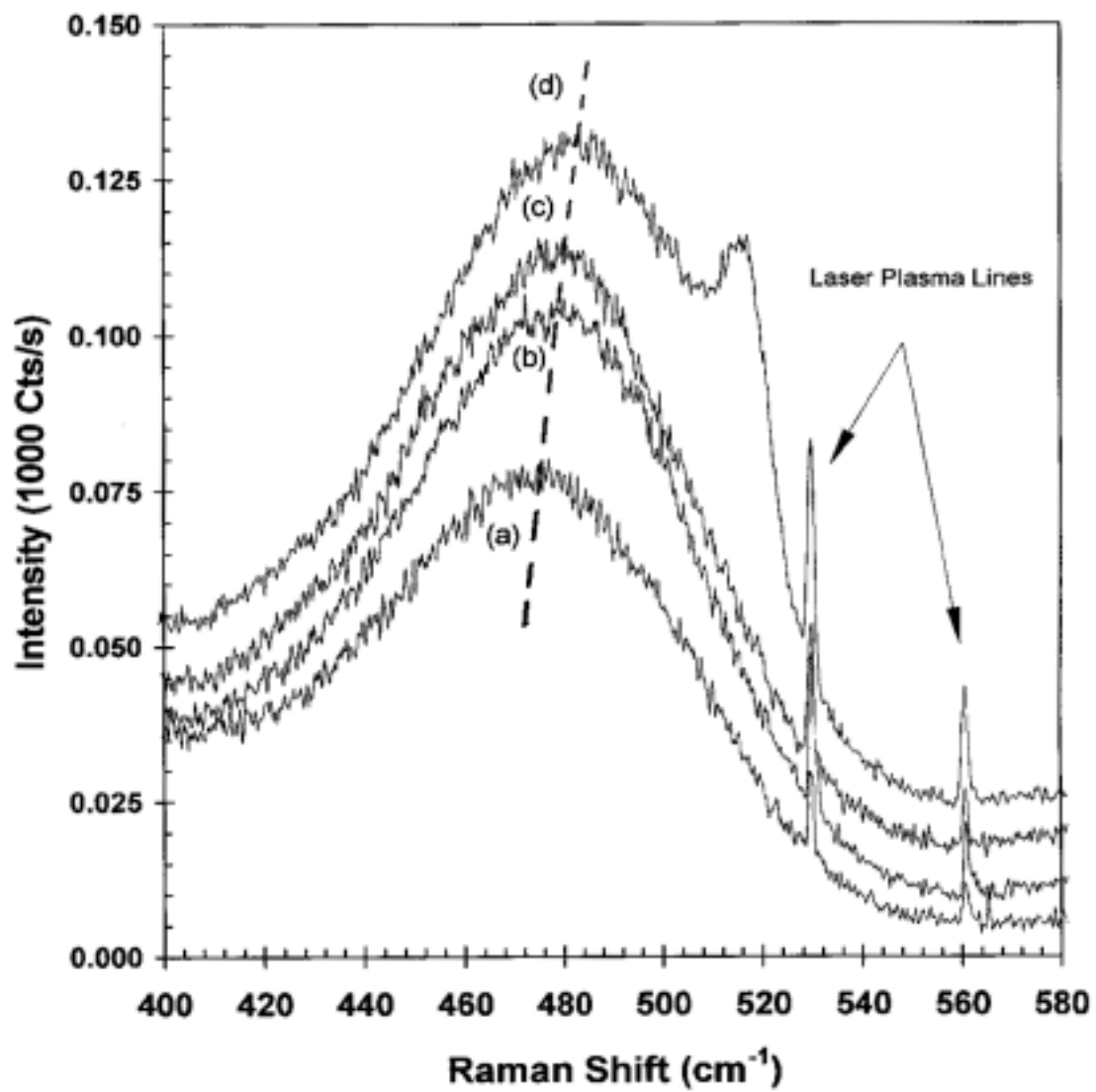**Figure 2. Deuterium evolution spectrum from the deuterated sample.**

Figure 3. Raman spectra versus hydrogen dilution of four samples: (a) no dilution, (b) low dilution, (c) medium dilution, and (d) high dilution.

degrees indeed exists in a-Si alloy films. The volume fraction occupied by microcrystallites within the amorphous material increases with increasing hydrogen dilution.

Recently, we have conducted a series of X-ray diffraction (XRD) studies on a-Si alloys prepared from various hydrogen dilutions to see if XRD signals can be correlated with hydrogen dilution ratios (Guha et al. 1999). We found that the full-width-at-half maximum (FWHM) intensity of the first X-ray diffraction peak is narrower in high hydrogen diluted samples than those in low or no hydrogen dilution samples. This confirms the improved medium range order for high dilution samples. A detailed account is given by Williamson (Williamson 1999).

Very recently, in collaboration with Mahan et al., we carried out systematic IR and H_2 evolution studies for hydrogen diluted samples. A careful analysis of the IR spectra revealed that the peak frequency of the Si-H wagging mode shifts downward from ~640 cm^{-1} to 620 cm^{-1} for high H_2 dilution. The 620 cm^{-1} frequency has been interpreted as being due to H bonded to the surfaces of very small, highly eccentric Si microcrystallites. These crystallites catalyze the crystallization of the remainder of the amorphous matrix upon annealing and resulting in the observed low temperature peak in the H_2 evolution spectrum. A more detailed description of this work is given by Mahan et al. (Mahan et al. 1999).

Kamei et al. (Kamei et al. 1999) recently investigated effects of embedded crystallites in hydrogenated amorphous silicon on light-induced metastable dangling bond defect creation. The crystalline-like nanostructures were obtained by using hydrogen dilution during film growth, confirming the observation by Tsu et al. (Tsu et al. 1997). They also found that inclusion of a small-volume fraction of crystallites into the amorphous matrix significantly suppresses defect creation against moderate light illumination. They propose that the mechanism of improved stability is related to the trapping/recombination of photocarriers by embedded crystallites.

From the above discussion, it should be clear that appropriate hydrogen dilution can create intermediate range order and improve material properties. However, dilution beyond certain critical value often results in excess microcrystallite inclusions and degrades solar cell performance. In fact, a-Si alloy *p i n* cells with excess hydrogen dilution give rise to low open-circuit voltages and poor cell performance. We should also point out that the threshold condition is system dependent. In one system, a dilution ratio of ten to one may be the optimum, while in a different system, one may need a very different ratio. Other deposition parameters, such as pressure, temperature, electrode spacing, chamber geometry, and gas flows, all affect the growth kinetics. In fact, conditions too close to the threshold may not be easily reproducible. They may be too sensitive to small variations in the deposition conditions, as shown by a recent work using real-time spectroscopic ellipsometry (Koh et al. 1998).

Near Threshold Solar Cell Performance

From the above discussion, one should recognize the importance of using appropriate hydrogen dilution in the PECVD process to optimize the deposition conditions so that high quality materials can be obtained near the amorphous to microcrystalline transition. We have followed this approach and studied four different types of solar cell structures shown in Fig. 4. These structures use stainless steel substrates and textured silver/zinc oxide as back reflectors. Figure 4(a) shows the basic *p i n* structure most commonly used to evaluate the quality of the a-Si alloy materials. To achieve high efficiency in this structure, not only does one need high quality intrinsic material such as those discussed above, but also other key requirements such as light trapping, transparent conductive oxide, and interface properties. The thickness of the intrinsic layer is also very important. If the intrinsic layer is too thick, cells will suffer large degradation due to the Staebler-Wronski effect (SWE) (Staebler et al. 1977). If the intrinsic layer is too thin, it does not absorb sufficient photons, thus resulting in low efficiencies. An optimum
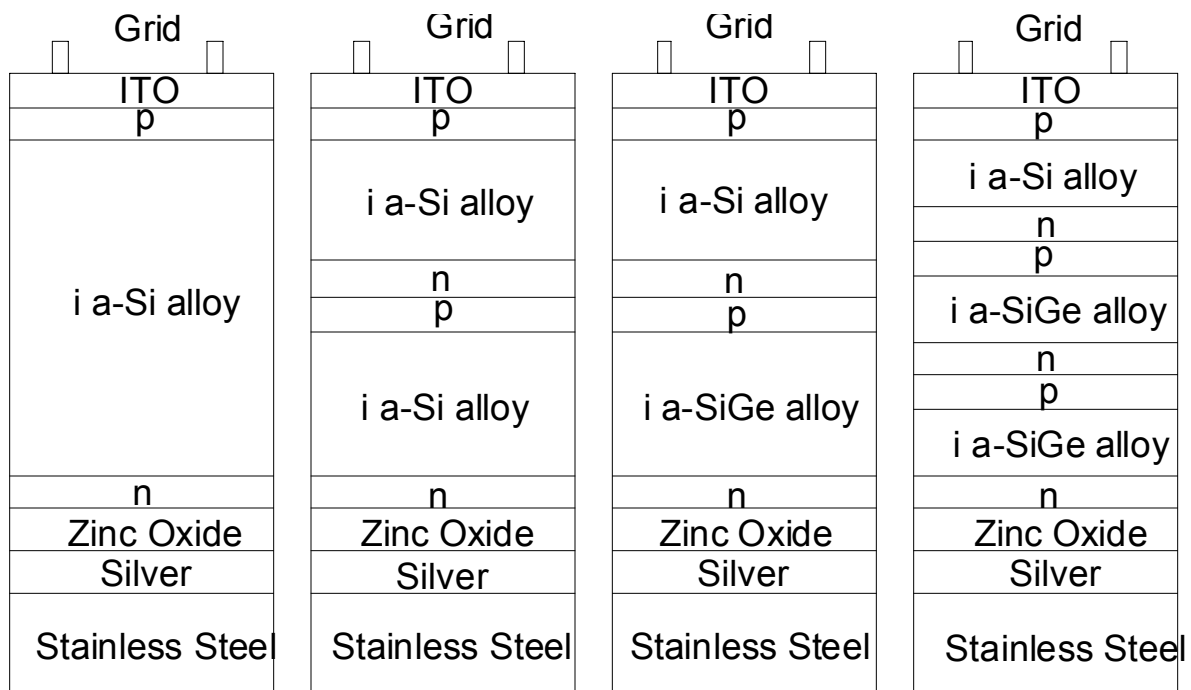
Grid Grid Grid Grid

(a) Single-Junction	(b) Same Gap Double-Junction	(c) Dual Gap Double-Junction	(d) Triple-Junction
ITO	ITO	ITO	ITO
p	p	p	p
i a-Si alloy	i a-Si alloy	i a-Si alloy	i a-Si alloy
	n	n	n
	p	p	p
	i a-Si alloy	i a-SiGe alloy	i a-SiGe alloy
			n
			p
			i a-SiGe alloy
n	n	n	n
Zinc Oxide	Zinc Oxide	Zinc Oxide	Zinc Oxide
Silver	Silver	Silver	Silver
Stainless Steel	Stainless Steel	Stainless Steel	Stainless Steel

(a) Single - Junction (b) Same Gap Double - Junction (c) Dual Gap Double - Junction (d) Triple - Junctio

Figure 4. Schematic diagram of four solar cell structures: (a) single, (b) same bandgap, double, (c) dual bandgap double and (d) triple junctions.

thickness of ~2200 Å was used to achieve the highest stabilized active-area efficiency of 9.3%. The initial and stable J-V characteristics are listed in Table 1. It should be pointed out that the degradation due to SWE for this structure is only 12.3%, a value much lower than the typical 50% degradation when the quality of the material was poor or the thickness of the intrinsic layer was too thick. Using hydrogen dilution during deposition, one generally observes less degradation and an earlier saturation (Yang et al. 1994, Yang et al. 1994).

For the same bandgap double-junction structure shown in Fig. 4(b), one takes advantage of the thin top cell. The thin top cell gives rise to a high internal field (Jiang et al. 1996), thus less degradation. The top cell also absorbs the high energy photons and allows only low energy photons to reach the bottom cell. From Table 1, we see that the initial fill factor of the same bandgap structure is higher than the single-junction structure; the stabilized fill factor is also higher. The stabilized efficiency of 10.1% is better than the 9.3% obtained from the single-junction structure.

Table 1. **Highest Stable Cell Efficiencies (active area ~0.25 cm^2) at United Solar for Different Junction Configurations.**

		J_{sc}	V_{oc}	FF	η	Deg.
		(mA/cm^2)	(V)		(%)	(%)
a-Si:H	Initial	14.65	0.992	0.730	10.6	
single junction	Stable	14.36	0.965	0.672	9.3	12.3
a-Si:H/a-Si:H	Initial	7.9	1.89	0.76	11.4	
same gap	Stable	7.9	1.83	0.70	10.1	11.4
double junction						
a-Si:H/a-SiGe:H	Initial	11.04	1.762	0.738	14.4	
dual gap	Stable	10.68	1.713	0.676	12.4	13.9
double junction						
a-Si:H/a-SiGe:H/	Initial	8.57	2.357	0.723	14.6	
a-SiGe:H	Stable	8.27	2.294	0.684	13.0	11.0
triple junction						

In order to further increase the cell efficiency, one resorts to narrow bandgap materials such as a-SiGe alloys to broaden the spectral response. The carrier transport properties in the a-SiGe alloy materials, however, are often worse than those in the a-Si alloys. Using the hydrogen dilution approach, we have been able to improve the performance of the a-SiGe alloy solar cells substantially. Hydrogen dilution also allows for a lower deposition temperature without deteriorating the fill factor of the device (Shima et al. 1997). Figure 5 shows the J-V characteristic of an improved a-SiGe alloy device having an average germanium concentration of ~20% in the intrinsic layer. The intrinsic layer has also incorporated a bandgap profiling design (Guha et al. 1989) to improve the cell performance. The 11.6% initial active-area efficiency is the highest reported to date for a single-junction a-SiGe alloy solar cell.
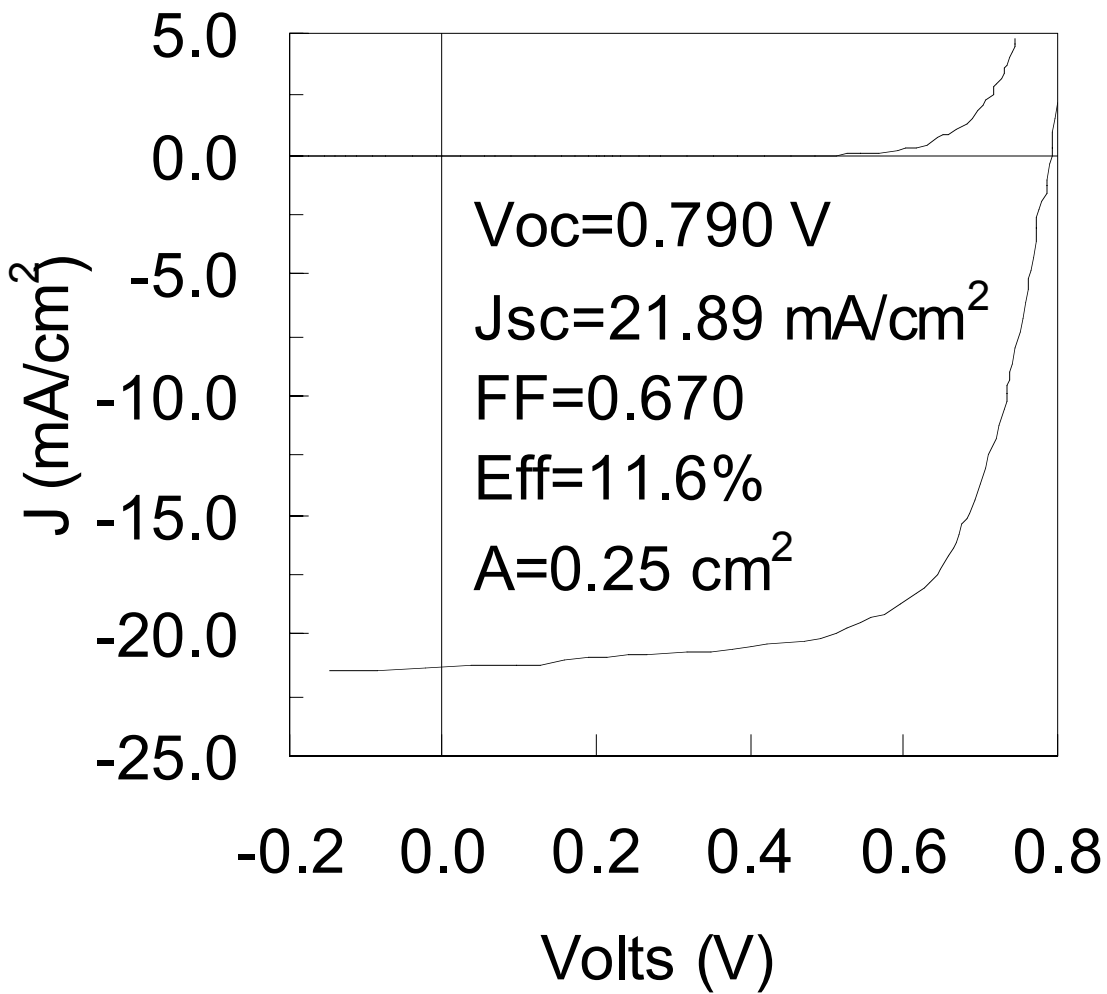
Figure 5. Initial J-V characteristic of an a-SiGe alloy *p-i-n* solar cell.

Using the improved a-SiGe alloy in the bottom cell, we then proceeded to make dual bandgap double-junction solar cells using the structure shown in Fig. 4(c). In this structure, the top cell needs to be thicker than that of the same gap structure in order to match the higher photocurrent generated by the a-SiGe alloy bottom cell. The initial and stable characteristics of the best dual gap double-junction cell is also shown in Table 1. Comparing the dual gap and same gap structures, it is obvious that the main advantage of the dual gap structure is the substantially higher current density, which overcomes the lower open-circuit voltage and fill factor. In fact, the dual gap structure shows a more than 20% gain in the stabilized efficiency than the same gap structure. The degradation of the dual gap device, on the other hand, is higher than the same gap counterpart. This is mainly due to the thicker top cell and the somewhat poorer a-SiGe alloy material in the bottom cell.

To further enhance the efficiency and broaden the spectral response, we next discuss the triple-junction configuration shown in Fig. 4(d). The structure incorporates a low bandgap a-SiGe alloy in the bottom cell. In this configuration, the bandgap and thickness of the top and middle cells are dictated by the quality of the bottom cell. If one can successfully incorporate a higher concentration of germanium into the bottom cell and further extend the spectral response into the long wavelength region, one may split the spectral response into blue, green, and red regions, corresponding to the top, middle, and bottom cells, respectively. The goal of this design is, of course, that the gain in current can overcome the loss in V_{oc} and FF. We have again used the hydrogen dilution method and successfully achieved 14.6% initial and 13.0% stable conversion efficiencies for a 0.25 cm^2 active-area device in the triple-junction configuration. Their J-V characteristics are also listed in Table 1. Figure 6 shows the J-V characteristic of the 14.6% triple-junction cell; the quantum efficiency versus wavelength plot for this device is shown in Fig. 7.

It should be pointed out that the stabilized efficiency for each structure in Table 1 represents the highest value reported to date in the literature. Hydrogen dilution indeed played a major role in achieving this result. We should also point out, however, that high quality material is a necessary but not sufficient condition for making high efficiency solar cells. Other key factors, such as the design of the device structure, the appropriate back reflector, the thickness and the optical bandgap of the intrinsic layer, the bandgap profiling of the a-SiGe alloys, the interface layers, the tunnel junctions, the component cell current matching, and the top conductive oxide, all play an important role in achieving the high efficiency cells (Yang et al. 1997).

Based on the experimental data of Table 1, it is easy to conclude that the triple-junction structure gives rise to the highest initial and stable efficiencies. The quantum efficiency curve in Fig. 7 clearly shows the spectral-splitting feature of the triple-junction design. The current mismatch observed among the three component cells is designed to limit the triple-junction current by the top cell which usually has the best fill factor. Any improvement in the fill factor of the middle or bottom cell can allow us to further reduce the current mismatch and improve the cell efficiency. Our continuous effort in optimizing the device design and deposition conditions has led us to achieve a 15.2% initial active-area efficiency. The J-V characteristic is shown in Fig. 8, and the quantum efficiency plot is shown in Fig. 9. From Fig. 9, one can see that the spectral response spans from below 350 nm to beyond 950 nm with the peak quantum efficiency exceeding 90% in the green region. The triple stack generates a total photocurrent of 27 mA/cm^2. The current mismatch among the component cells has been virtually eliminated.

Based on the above experimental results and discussion, it is clear that hydrogen dilution improves the microstructure and enhances the cell performance. The optimum condition is very close to the amorphous to microcrystalline transition. The challenge is to approach the threshold without exceeding the critical limit. In order to find out the cell characteristics at optimum conditions, we have evaluated a series of a-Si alloy top cells on stainless steel substrates by adjusting the hydrogen dilution

Voc=2.357 V

Jsc=8.57 mA/cm^2

FF=0.723

Eff=14.6%

A=0.25 cm^2
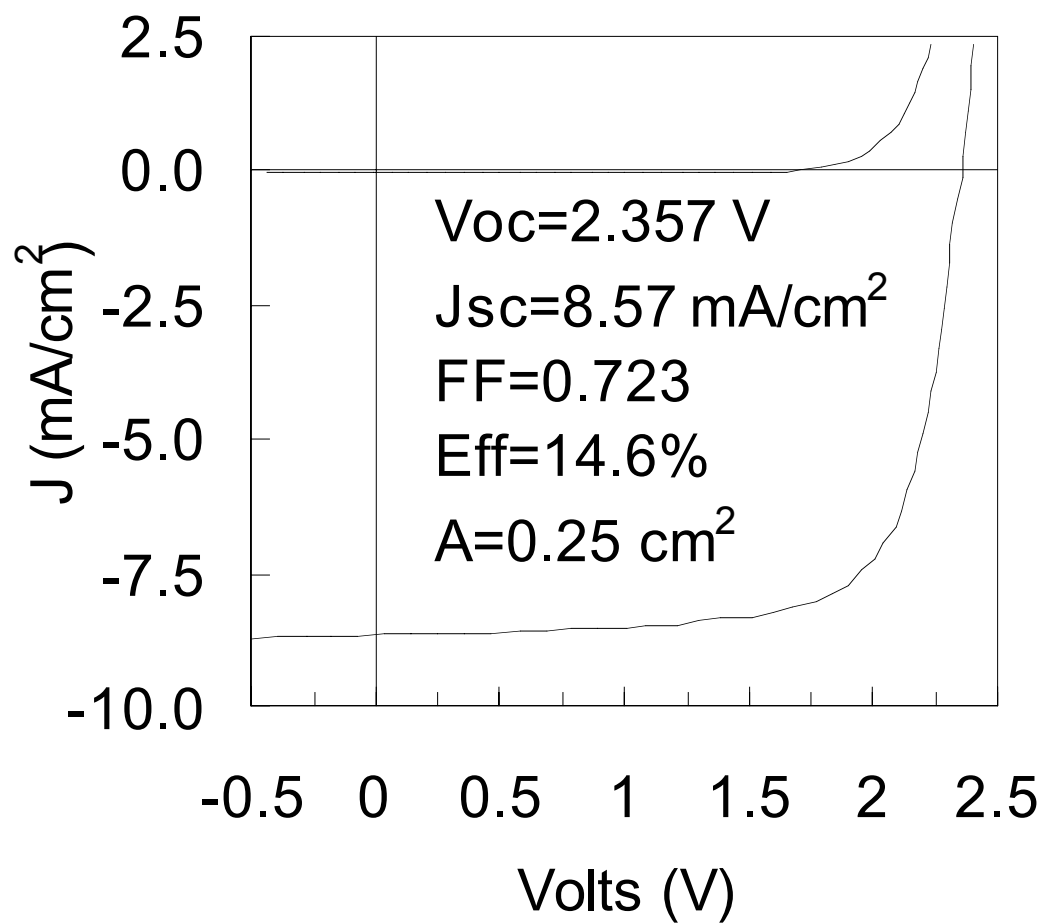
Figure 6. Initial J-V characteristic of the 14.6% triple-junction cell.
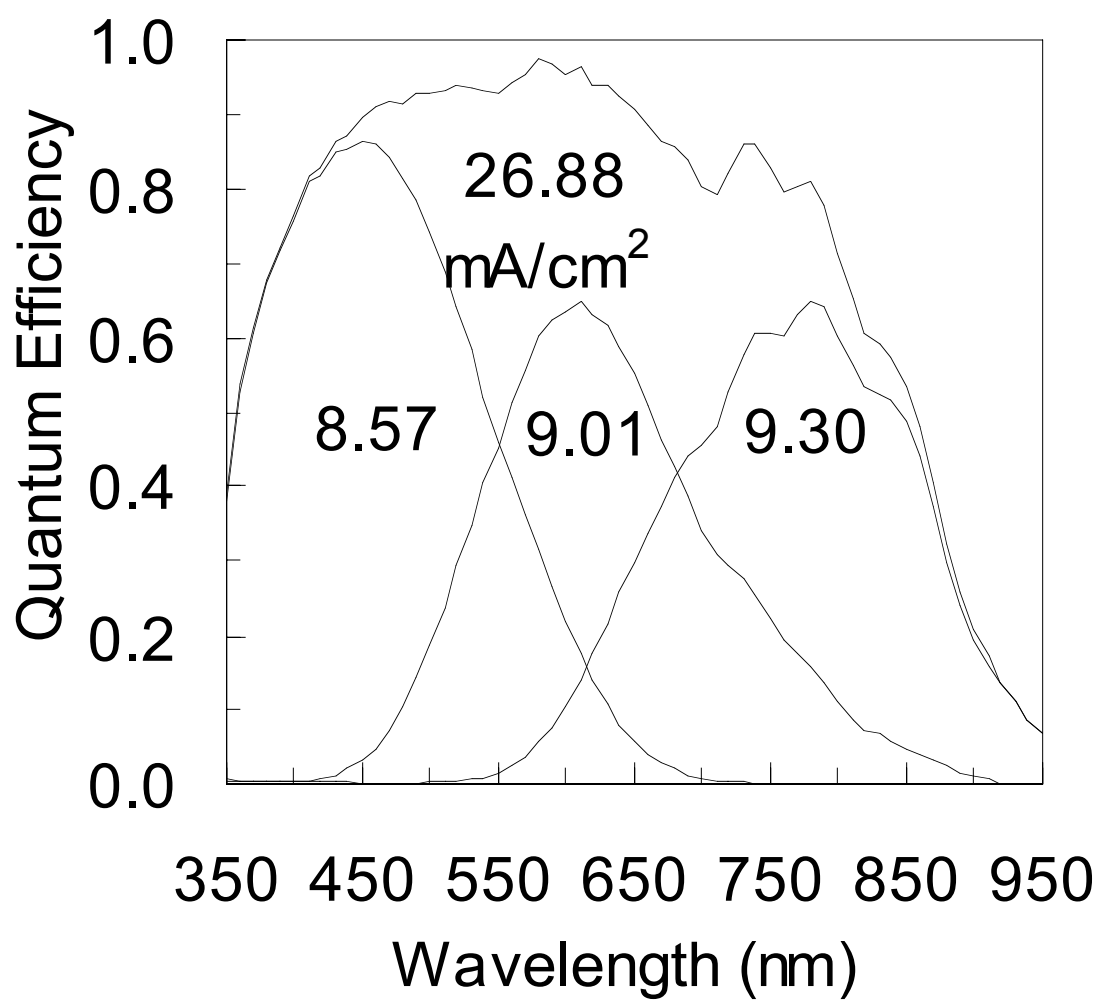
Figure 7.   Quantum efficiency of the device shown in Fig. 6.
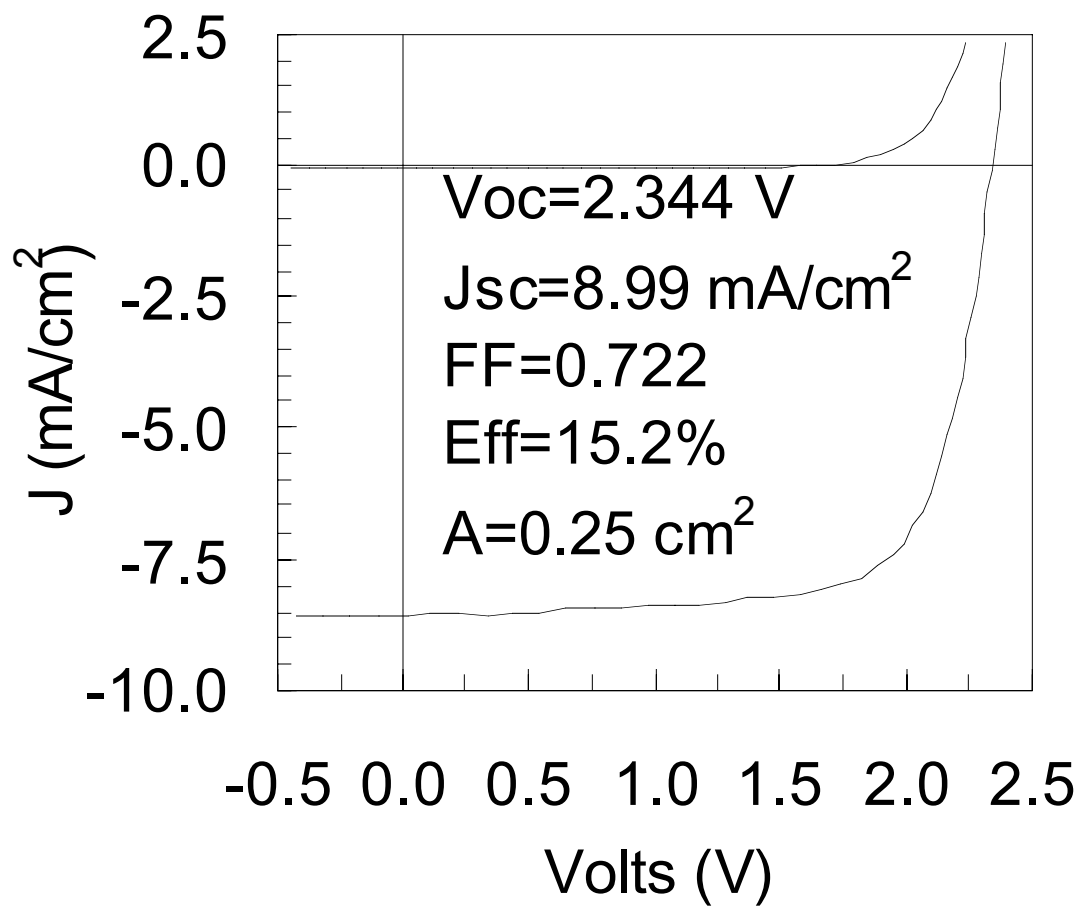
Figure 8. Initial J-V characteristic of the 15.2% triple-junction cell.
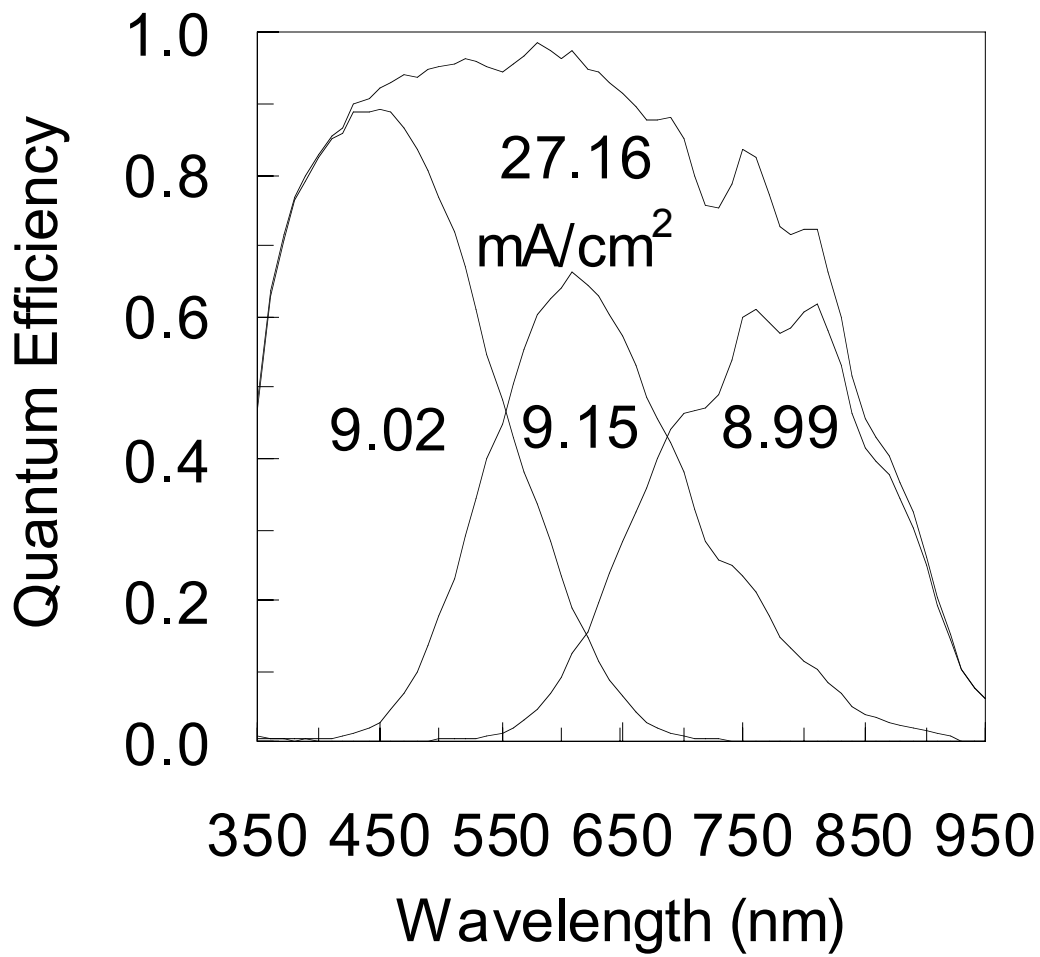
Figure 9. Quantum efficiency of the device shown in Fig. 8.

condition near the threshold. The requirement is that the J_{sc} value must be around 8 mA/cm^2 for top cell applications. Figure 10 shows the best cell obtained to date in terms of high fill factor and high open-circuit voltage. The cell exhibits FF = 0.785, V_{oc} = 1.010 volt, and J_{sc} = 8.25 mA/cm^2. As soon as the dilution ratio exceeds a certain critical value, a sudden drop in FF and V_{oc} occurs, signifying that the threshold has been exceeded.

Hydrogen dilution in general lowers the deposition rate. The high efficiency cells described above have a typical deposition rate of ~1 Å/s. Can one obtain high quality materials and solar cells using high deposition rates? This is of particular interest concerning the throughput in large volume productions. We have used a modified very high frequency (MVHF) approach and studied the hydrogen dilution effect on high-rate-deposited top cells (Yang et al. 1998). More detail is discussed in Section 3. Figure 11 shows the best cell obtained to date using MVHF with hydrogen dilution at a deposition rate of 8 Å /s. The J-V characteristic is very close to that of the 1 Å /s cell shown in Fig. 10. High performance a-Si alloy cells can indeed be achieved at high rates using an appropriate hydrogen dilution. More work is needed to study the a-SiGe alloy using high deposition rates.

Summary

Using hydrogen dilution during film growth in the PECVD process, we have shown that the microstructure of the material and solar cell performance are improved. Interesting features associated with hydrogen diluted films near the amorphous to microcrystalline transition are reviewed. They include the observation of linear-like objects in the TEM micrograph, a shift of the principal Si TO band in the Raman spectrum, a low temperature H_2 evolution peak, a shift in the wagging mode frequency in the IR spectrum, and a narrowing of the Si (111) peak in the X-ray diffraction pattern.

World record high efficiency solar cells in four different device structures have been achieved by optimizing hydrogen dilution conditions near the threshold of the amorphous to microcrystalline transition. More work is needed to understand these hydrogen diluted materials to improve the efficiencies further.

Voc=1.010 V

Jsc=8.25 mA/cm^2

FF=0.785

Eff.=6.54%

A=0.25 cm^2
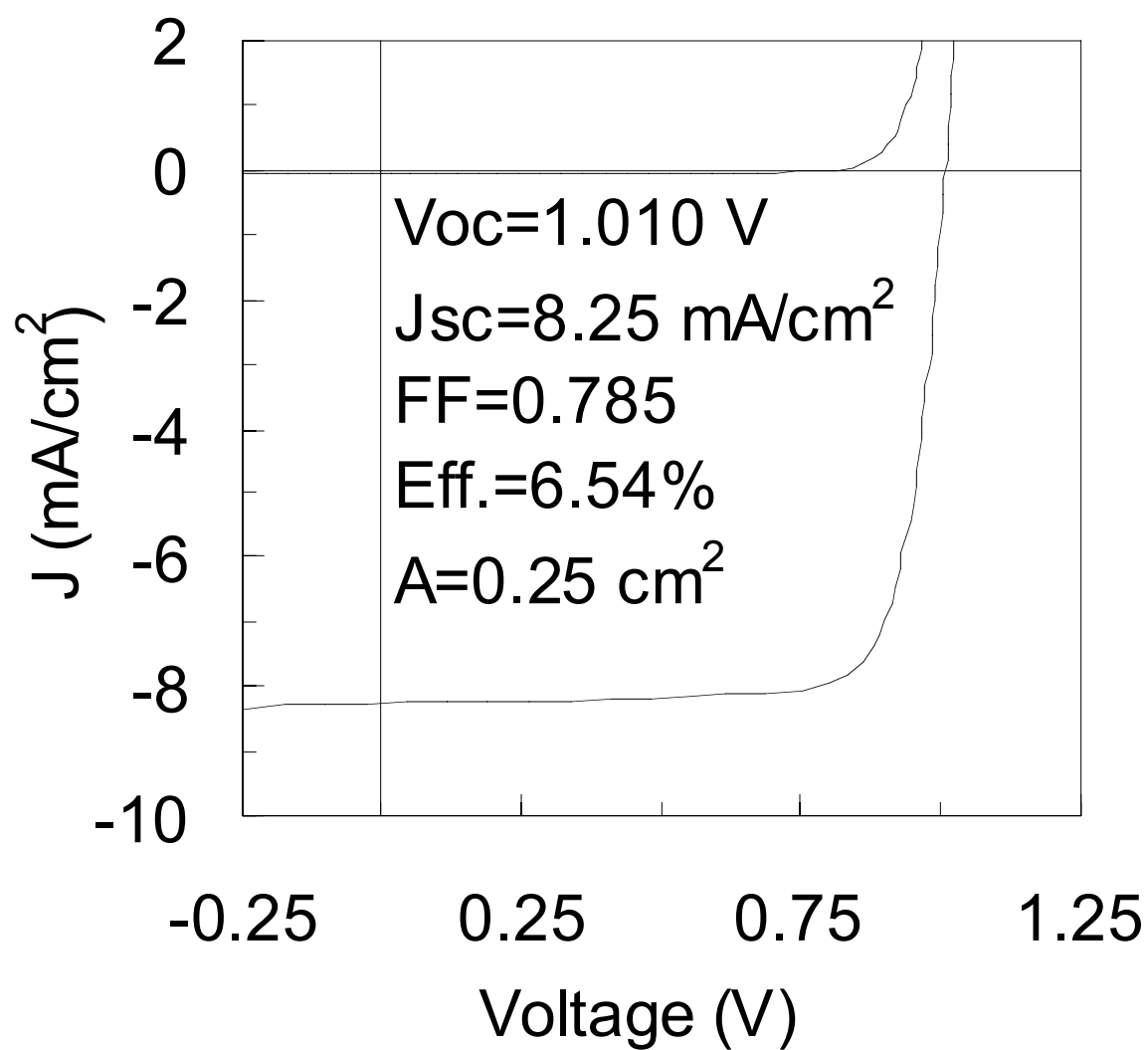
Figure 10. Initial J-V characteristic of an a-Si alloy top cell deposited at ~1 Å/s.

Voc=0.995 V

Jsc=8.34 mA/cm^2

FF=0.749

Eff.=6.22%

A=0.25 cm^2

Figure 11. Initial J-V characteristic of an a-Si alloy top cell deposited at ~8 Å/s by MVHF.

Section 3

Status of Small Area Component and Multi-junction Cells Deposited with RF and MVHF at 3~5 Å/s

Introduction

Investigations are underway to increase the stabilized total area efficiency of triple-junction solar cells deposited at both high rate, 3 - 5 Å/s, and low rate, 1 Å/s. Higher deposition rates are attractive because of increased throughput and reduced manufacturing costs. To achieve higher deposition rates, both RF (13.56 MHz) and MVHF (75 MHz) PECVD are being investigated. In an earlier study, we have shown that an increase in the deposition rate of a-Si alloys using 13.56 MHz resul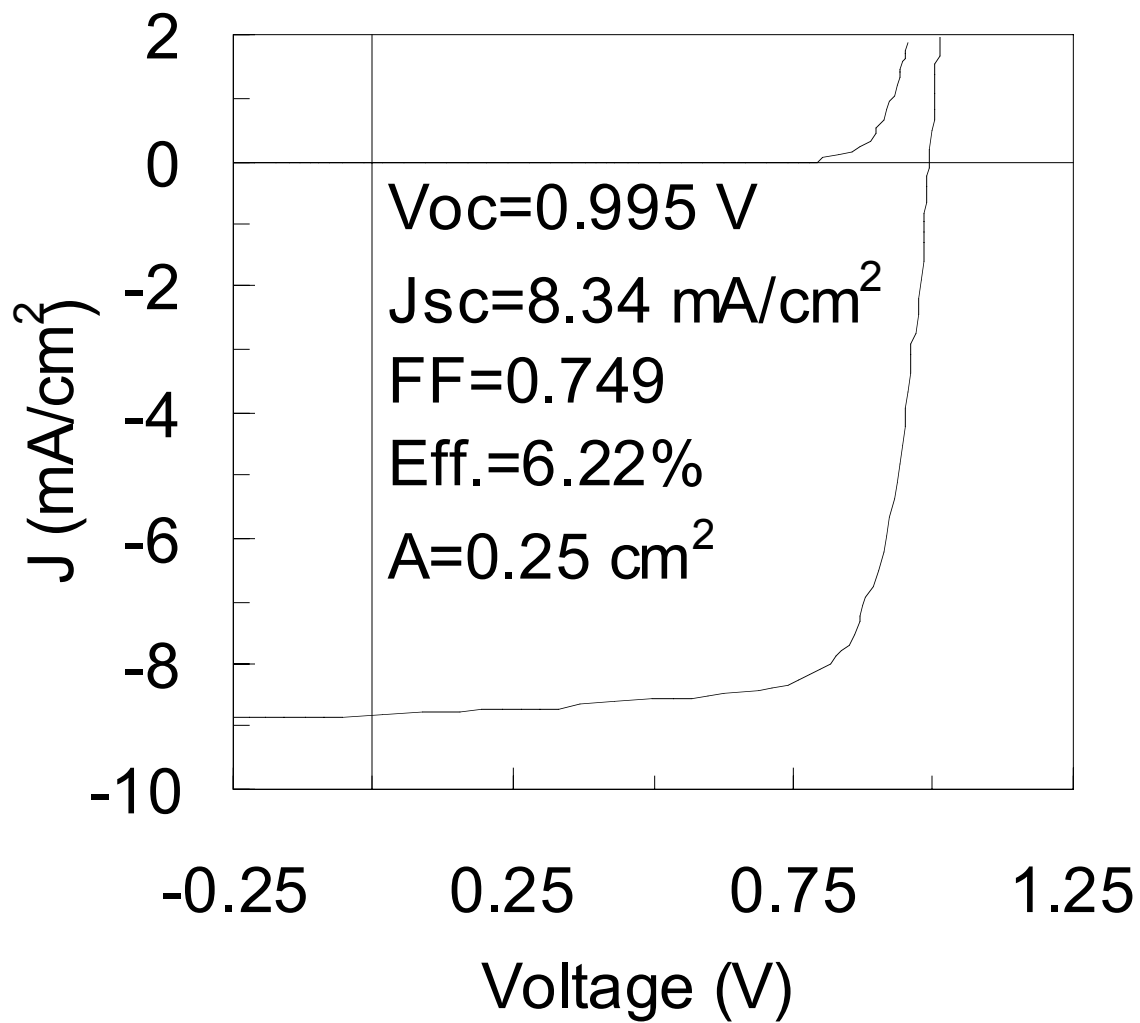ted in an increase in microvoid density, which is believed to cause a poorer cell performance and stability (Guha et al. 1992). On the other hand, we have also found that the microstructure of the material depends critically on the deposition conditions such as the degree of hydrogen dilution during the film growth (Tsu et al. 1997). Moreover, solar cells made using a 2.45 GHz microwave excitation with a deposition rate of ~100 Å/s have given high initial efficiencies (Guha et al. 1995). An optimum deposition condition for high quality materials may exist for a given excitation frequency. Currently, the highest stabilized efficiencies are deposited with a conventional RF-PECVD at rate of 1 Å/s. Initial and stabilized active area efficiencies of 14.6% and 13.0% have been reported (Yang et al. 1997). The initial performance of single-junction a-Si alloy cells fabricated by MVHF at 6 Å/s is similar to RF at 3 Å/s. However, the stability of a-Si alloy MVHF cells is superior to the 3 Å/s RF top cells. High deposition rate a-SiGe alloy middle cells fabricated with RF and MVHF exhibit similar characteristics. MVHF bottom cells currently exhibit inferior initial and stabilized performance than the RF bottom cells. Experiments are being conducted to identify the source of the deficit in the MVHF bottoms cells deposited faster than 3 Å/s and are discussed in detail below.

Status of 3 Å/s RF a-Si Alloy Solar Cells

Efforts are being made to increase the total area efficiencies of the single-junction component cells deposited by 13.56 MHz RF at 3Å/s. The small area cells have a total area of 0.268 cm^2 and an active area of 0.25 cm^2. Top and middle component cells are deposited on bare stainless steel. Bottom cells are deposited onto a textured AgZnO back reflector. Top cells are measured under AM1.5 illumination. Middle cells are measured under AM1.5 illumination with a 530 nm cut on filter, and bottom cells are measured with a 630 nm cut on filter. A stabilized total area efficiency of 4.70% has been reported for the top cell and meets the Phase I goal. A stabilized total area p_{max} of 2.80 mW/cm^2 for the middle cell and 3.20 mW/cm^2 for the bottom cell have also been previously reported. In the course of this phase, middle cell B4410 with an initial total area p_{max} of 3.91 mW/cm^2, and stabilized p_{max} of 2.80 mW/cm^2 has been fabricated. The bottom cell, B4030, with an initial total area p_{max} of 3.80 mW/cm^2 and a stabilized p_{max} of 3.11 mW/cm^2 has been fabricated, and meets the Phase I goal.

The characteristics of triple-junction a-Si alloy cells deposited by RF at 3 Å/s are reported. B3363, a triple-junction cell, has an initial AM1.5 total area efficiency of 11.7% and a stabilized total area efficiency of 9.5%. The stabilized efficiency is to be improved to 10.7% to meet the proposed Phase I goal. Currently, the single-junction top and bottom component cells meet the proposed stabilized total area Phase I goal of 4.7% and 3.0 mW/cm^2, respectively. However, the middle and triple-junction cells are to be improved. Investigations are underway to reduce the degradation in the middle cell.

Modified Very-High-Frequency Plasma Enhanced Chemical Vapor Deposition (MVHF-PECVD): Plasma Properties and Solar Cell Deposition

Introduction

Ten years ago, Chatham and Bhat (Chatham et al. 1989) used very-high-frequency (VHF) PECVD to deposit a-Si alloy solar cells at high deposition rates. They demonstrated an efficiency of 9.7% for an a-Si alloy solar cell made at 18 Å/s using a frequency of 110 MHz. Since then, many groups have used this technique to deposit a-Si alloy materials and devices. The group at Utrecht studied the properties of the VHF plasma (Harmers et al. 1997) and deposited a-Si alloy solar cells (Van Spark et al. 1996) and thin film transistors. They reached an initial efficiency of 10% (Van Spark et al. 1996). The group at Neuchâtel showed that VHF-PECVD has advantages to make microcrystalline silicon (μc-Si) at rates much higher than ordinary RF plasma deposition of μc-Si (Shah et al. 1997). They deposited μc-Si solar cells and a-Si/μc-Si tandem solar cells.

In our laboratory, we have used an MVHF-PECVD (refer to MVHF) system to deposit a-Si and a-SiGe alloy solar cells. We found that a-Si alloy solar cells made with MVHF at 6 Å/s show similar initial performance as those made with RF at 3 Å/s, and the stability of 6 Å/s MVHF cells is better than the 3 Å/s RF cells (Yang et al. 1998). To further improve the performance of the MVHF solar cells made at high deposition rates, we need to understand the difference in the plasmas excited by RF and MVHF, and search for further improvement of the solar cells. For this purpose we have systematically studied the ion energy distribution of MVHF and RF plasmas as well as the effects of ion bombardment on the performance of a-Si and a-SiGe alloy solar cells. It has been shown that high H_2 dilution can improve the performance and stability of a-Si alloy solar cells made with RF plasmas at low deposition rates (Guha et al. 1981). However, the effect of H_2 dilution on the solar cells made with MVHF at high rates are not clear. Recent studies on the effects of H_2 dilution on the a-Si and a-SiGe alloy solar cells are summarized in the last sub-section.

Experimental

A parallel plate capacitance reaction chamber (MVHF chamber), which was adapted to a multi-chamber PECVD system, was designed to have the capability to couple RF (13.65 MHz) and VHF (75 MHz) frequencies to the plasma. The substrate can be grounded, externally biased or floated, which gives us the flexibility to study the effects of ion bombardments. A retarding field analyzer was installed in the plasma chamber to measure the energy distribution of positive ions. The details of the ion energy distribution experiments are presented elsewhere (Yan et al. 1999). The ion energy distributions of H_2, Ar, SiH_4 and their mixtures were studied as functions of excitation frequency, RF or VHF power density and pressure. a-Si and a-SiGe alloy component cells were made with various conditions, such as different pressures, gas flow rates, substrate temperatures and external biases, to optimize their performance and to improve the tandem and triple junction cells.

Ion energy distribution and the effects of ion bombardments on a-Si alloy solar cells

Figure 12 shows the energy distribution of ions in H_2 plasma with 75 MHz excitation, where the VHF power was 10 W. At a low pressure (0.1 Torr), a sharp peak appears at 22 eV with a full width at half-maximum of about 6 eV. The cut-off at the high energy side is very sharp. This value could be the plasma potential. However, at high pressure (1.0 Torr), the peak of ion energy distribution shifts to zero and the width becomes significantly broader. Similar measurements were carried out for the RF plasma. Figure 13 shows the results of the RF plasma with the same conditions as in Fig. 12 except the excitation
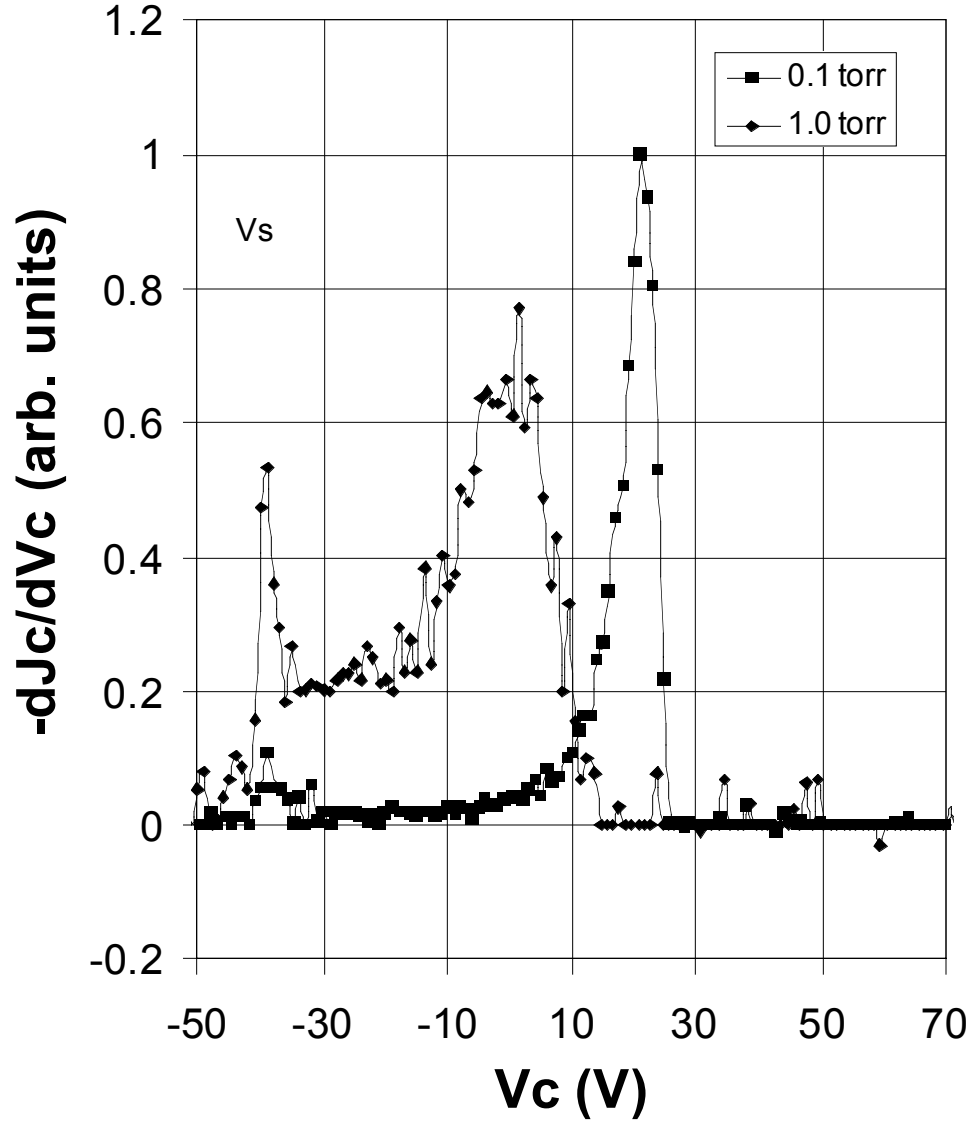
Figure 12. The energy distribution of positive ions reached to the substrate in a H_2 plasma excited by 75 MHz VHF. The pressures were 0.1 and 1.0 Torr and VHF power was 10 W.
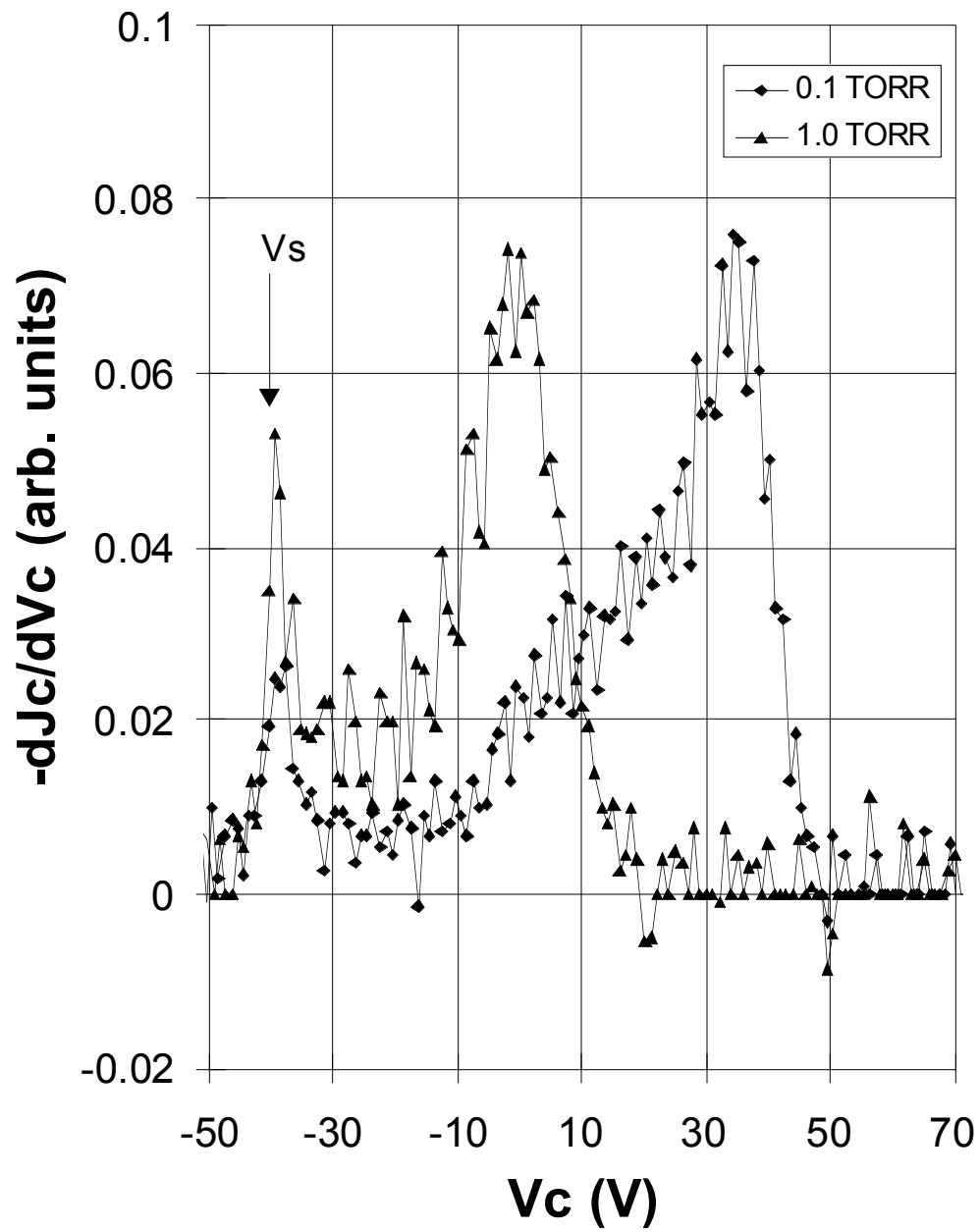
Figure 13. The positive ion energy distribution of a H₂ plasma excited by 13.56 MHz RF. Other conditions are the same as in Fig.12.

frequency was 13.56 MHz. The peak position is much higher (37 eV) than that shown in Fig. 12, and the distribution is also much broader (18 eV). Similar to the MVHF plasma, there are no high energy ions reaching the substrates at 1.0 Torr. In addition, the positive ion current that reached the substrate is about 5 times higher in the 75 MHz MVHF plasma than in the RF plasma.

The shifting and broadening of the ion energy distribution with the increase in pressure could result from the collision of positive ions with neutral species when the ions travel through the sheath. The collision not only transfers energy to neutral species but also has a probability to exchange charge. The charge-exchange collision yields low energy neutral radicals and reduces the energy of the ions as measured by the retarding field analyzer. This process is significant in Ar plasma since the charge-exchange collision cross section is very large for argon ions (Gallagher 1999). Experimentally, we found that the ion energy distribution collapsed even at low pressure for Ar plasma (0.1 torr).

Compared with pure H_2 plasma, a mixture of SiH_4 and H_2 shifts the ion energy distribution to a lower energy, as shown in Fig. 14. This shift probably indicates that the plasma potential is higher for pure H_2 plasma than for the plasma with H_2 and SiH_4 mixture. This phenomenon is similar for both RF and MVHF plasmas.

The increase of excitation power slightly shifts the energy distribution of MVHF plasma to a higher energy as shown in Fig. 15. The shape of the ion energy distribution remains unchanged within the experimental errors. It probably means that the plasma potential is increased by the high power since the peak-to-peak voltage increases with the increase of power level. However, for a RF plasma there is no significant change at the cut-off energy, instead the shape of the distribution is changed. Figure 16 compares the ion energy distributions for an RF plasma with 3 W and 30 W. Because the plots are in arbitrary units, we may only say that the ratio of the high energy peak to the broad low energy shoulder increases with the increase of RF power. The mechanism responsible for the difference in the power dependence between RF and MVHF is not clear at this stage.

From the ion energy distribution measurements we have learned the following. First, the ion bombardment occurs only at low pressures. For normal solar cell deposition pressures, there is no significant ion bombardment from the plasma itself. Second, at low pressures, the ion bombardment is higher in RF plasma than in MVHF plasma. Third, the positive ion flux is higher in MVHF plasma than in RF plasma.

In order to find out whether the ion bombardment is beneficial for making a-Si alloy solar cells with MVHF, we have performed systematic studies of the effects of pressure and external bias on a-Si alloy solar cells. Table 2 lists the characteristics of a-Si alloy solar cells deposited on stainless steel with a thickness of around 2100 Å, where the intrinsic layers were deposited at different pressures. The deposition rate is significantly influenced by the pressure. The cell made at 0.1 Torr is not as good as the cells made at 1.0 Torr or 1.5 Torr although the deposition rate is only 4.4 Å /s. This is probably due to the ion bombardment. On the other hand, at pressures higher than 2.0 Torr, the V_{oc} and FF drop, which may have resulted from the polymerization in the plasma.

Table 3 summarizes the performance of a-Si alloy solar cells deposited at 0.1 Torr with different external DC biases. The positive and negative biases slightly reduce and enhance the deposition rate, respectively. The FF of the positively biased cells is better than the one deposited on a floating substrate. The negative bias significantly reduces the FF. Physically, a positive bias reduces the energy and flux of the positive ions and a negative bias accelerates the positive ions toward the substrate. Therefore, we may conclude that ion bombardment is not beneficial for making a-Si alloy solar cells using our MVHF with current conditions.
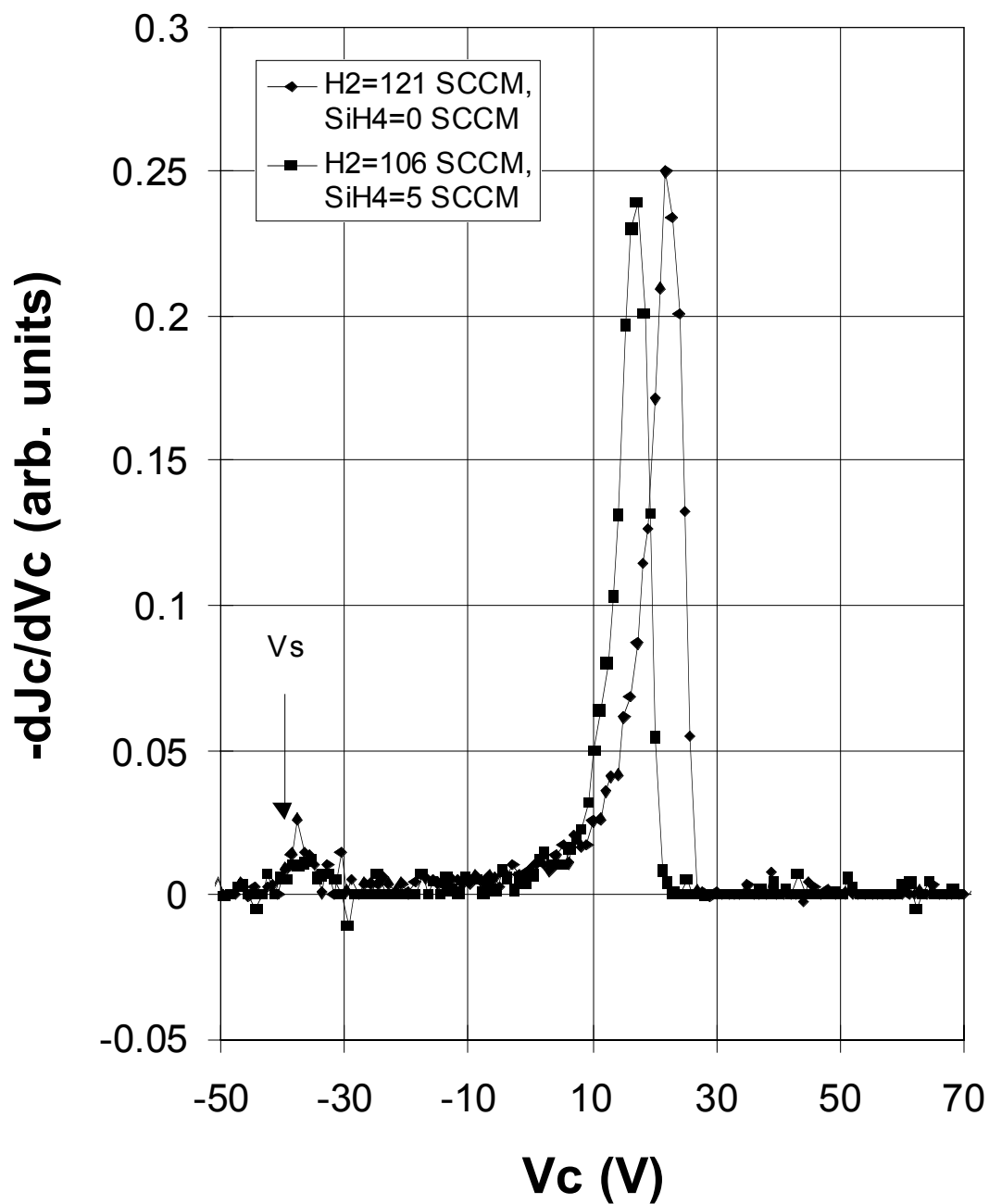
Figure 14. Comparison of the positive ion energy distribution of pure H$_2$ plasma and plasma with H$_2$ and SiH$_4$ mixture. The measurements were made at 0.1 torr with 11 W VHF power.
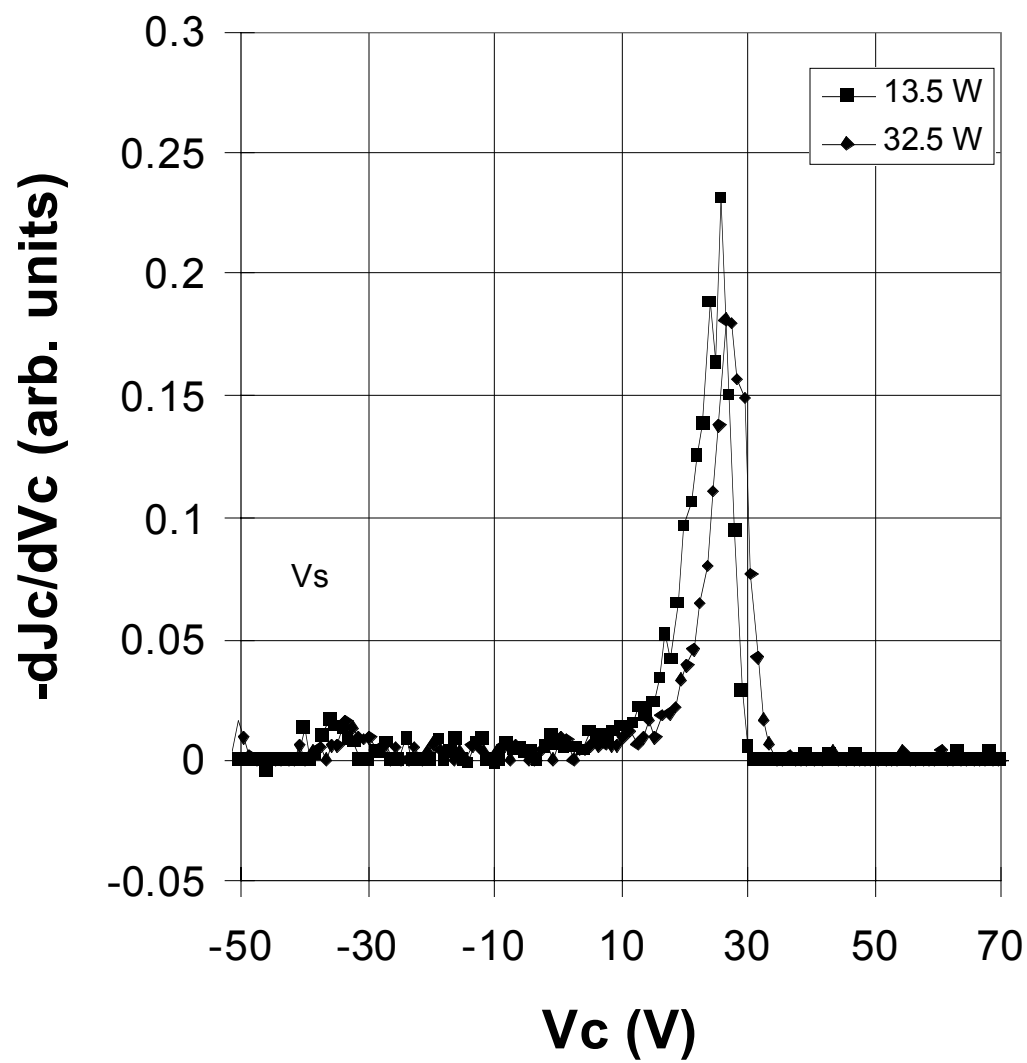
Figure 15. Ion energy distribution with two VHF powers for a H$_2$ plasma at 0.1 torr.
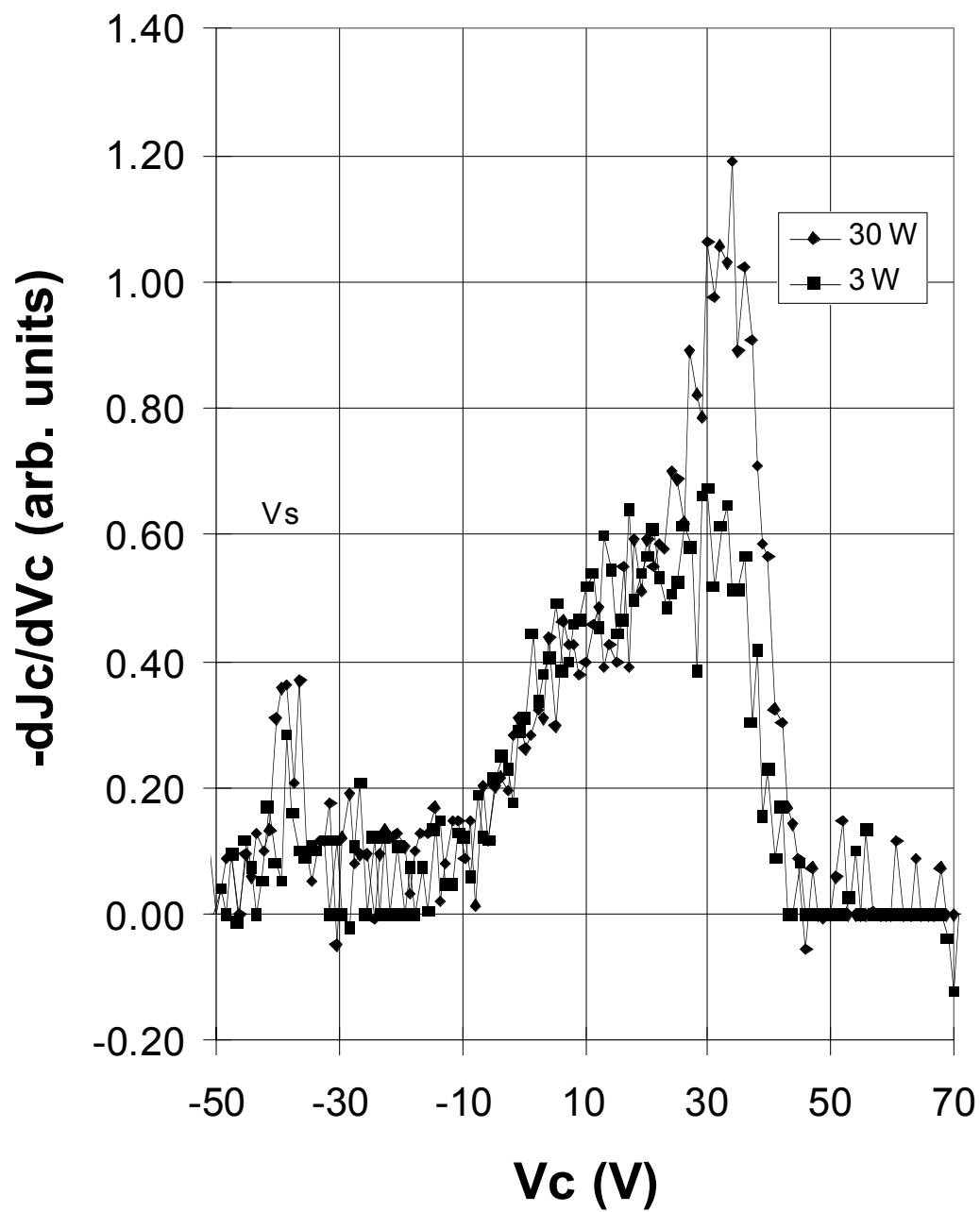
Figure 16. Ion energy distribution with two RF powers for a H_2 plasma at 0.1 torr.

Table 2. Characteristics of a-Si Alloy Solar Cells Made at Different Pressures.

Sample	J_{sc} (mA/cm^2)	V_{oc} (V)	FF	FF$_b$	FF$_r$	Efficiency (%) Active	Total	Rate (Å/s)	d (Å)	Pressure (Torr)
VHF7666	9.75	0.991	0.698	0.767	0.684	6.74	6.27	4.4	2170	0.1
VHF7689	11.2	0.976	0.702	0.759	0.706	7.66	7.12	14.0	2530	1.0
VHF7664	10.55	0.990	0.719	0.781	0.706	7.41	6.89	8.9	2135	1.5
VHF7687	9.91	0.956	0.701	0.770	0.704	6.23	5.79	6.0	1810	2.0
VHF7694	11.04	0.936	0.646	0.771	0.694	6.67	6.20	3.0	2085	2.5

Table 3. Characteristics of a-Si Alloy Solar Cells Made at 0.1 Torr with Different Biases.

Sample	J_{sc} (mA/cm^2)	V_{oc} (V)	FF	FF$_b$	FFr	Efficiency (%) Active	Total	Rate (Å/s)	d (Å)	Bias (V)
VHF7716	9.67	0.989	0.695	0.759	0.681	6.64	6.18	4.2	2040	-5.6*
VHF7717	9.84	0.998	0.702	0.778	0.689	6.89	6.41	4.1	2000	+30
VHF7718	9.65	0.999	0.714	0.774	0.689	6.88	6.40	4.0	1980	+60
VHF7738	9.74	1.000	0.705	0.767	0.679	6.87	6.39	4.1	2000	+90
VHF7739	9.49	0.997	0.712	0.770	0.700	6.74	6.27	3.9	1930	+120
VHF7740	9.48	1.005	0.721	0.780	0.695	6.87	6.39	3.9	1930	+150
VHF7741	9.08	0.992	0.632	0.711	0.671	5.69	5.29	4.7	2280	-60
VHF7742	8.42	1.005	0.617	0.691	0.635	5.22	4.85	4.9	2410	-120

*Self bias on floating substrate.

30

The pressure and external bias experiments were also carried out on a-SiGe alloy middle cells. The performance of middle cells is strongly dependent on pressure. The cells made at low pressure (0.1 Torr) show relatively poor performance. However, the external bias probably has more effect at low pressures than at high pressures. Therefore, we first made a-SiGe alloy middle cells at a low pressure with different biases on the stainless steel substrate. The characteristics of these cells are listed in Table 4, where the measurements were made under an AM1.5 solar simulator with a 530 nm cut-on filter. The negative bias increases V_{oc} and decreases J_{sc}, which probably means that less Ge is incorporated into the a-SiGe alloy layer. The positive bias has very little effect on the performance of the cell. Since our current best a-SiGe alloy cell is made at high pressure, we examine the bias effect for high pressure cells. The results are listed in Table 5. Similar to the low pressure case, the positive bias does not affect the cell performance, but the negative bias reduces the FF. It should be pointed out, however, the negatively biased cells are slightly thicker than the unbiased and positively biased cells.

Table 4. Characteristics of a-SiGe Alloy Middle Cells Made at Low Pressure with External Bias.

Sample	J_{sc} (mA/cm^2)	V_{oc} (V)	FF	FF_b	FF_r	P_{max} (mW/cm^2)		d (Å)	V_{bias} (V)
						Active	Total		
VHF7763	7.3	0.697	0.579	0.637	0.567	3.0	2.8	1410	-6.2*
VHF7766	7.0	0.699	0.579	0.623	0.578	2.8	2.6	1493	+60
VHF7775	7.2	0.688	0.562	0.593	0.561	2.8	2.6	1484	+120
VHF7767	4.7	0.812	0.625	0.671	0.613	2.4	2.2	1471	-60
VHF7776	6.3	0.762	0.612	0.632	0.606	2.9	2.7	1493	-120

*Self bias on floating substrate.

Table 5. Characteristics of a-SiGe Alloy Middle Cells Made at High Pressure with External Bias.

Sample	J_{sc} (mA/cm^2)	V_{oc} (V)	FF	FF_b	FF_r	P_{max} (mW/cm^2)		d (Å)	V_{bias} (V)
						Active	Total		
VHF7788	8.34	0.751	0.648	0.696	0.659	4.06	3.78	1675	-7.2*
VHF7801	8.71	0.739	0.618	0.679	0.635	3.98	3.70	1630	-6.7*
VHF7802	8.46	0.747	0.640	0.701	0.644	4.04	3.76	1620	+30
VHF7803	8.49	0.739	0.638	0.697	0.645	4.00	3.72	1710	+60
VHF7789	8.48	0.735	0.638	0.686	0.652	3.96	3.68	1665	+120
VHF7804	8.64	0.736	0.625	0.685	0.632	3.97	3.69	1630	-30
VHF7805	8.76	0.736	0.587	0.686	0.592	3.78	3.52	1740	-60
VHF7790	8.39	0.731	0.572	0.690	0.579	3.51	3.26	1715	-120

*Self bias on floating substrate.

Effects of Hydrogen Dilution on a-Si and a-Si alloy Solar Cells

H_2 dilution has been found to improve the performance and stability of RF a-Si alloy solar cells. The best a-Si and a-SiGe alloy solar cells were made with a hydrogen dilution level just below the threshold of microcrystalline silicon formation (Yang et al. 1999). The effects of H_2 dilution on the MVHF solar cells may be different for RF. The red FF drops with the increase of H_2 dilution within a certain range. This indicates that high H_2 dilution is not beneficial to making good material and devices in the range investigated. To clarify the different effects of H_2 dilution between RF deposition and MVHF deposition, systematic studies of H_2 dilution on a-Si and a-SiGe alloy solar cells were conducted.

The characteristics of a-Si solar cells made with different SiH_4 flow rates are plotted in Fig. 17, where all other deposition parameters were kept the same. These cells were designed to have an intrinsic layer thickness of about 2100 Å. It is clear that when the SiH_4 flow is lower than 4 sccm, all the parameters, J_{sc}, V_{oc} and FF, drop with a decrease of SiH_4 flow rate. This phenomenon probably relates to the formation of microcrystallites. For these experimental conditions, the threshold level of microcrystallization is around 4 sccm. The FF under AM1.5 and under red light increases with an increase in SiH_4 flow rate above 4 sccm. Meanwhile, J_{sc} slightly increases and V_{oc} slightly decreases. The cell made with a SiH_4 flow rate of 8 sccm exhibits the best overall performance with the other deposition parameters kept the same. In addition, the deposition rate increases with an increase in the SiH_4 flow rate. For a SiH_4 flow rate of 2 sccm, the deposition rate was 4.2 Å/s, while it was 8.8 Å/s for a flow rate of 10 sccm.

Similar experiments were made on a-SiGe alloy middle cells with a thickness of about 1500 Å. The cells were deposited on stainless steel (SS) and on Ag/ZnO back reflector (BR). For this study, we kept the deposition rate ~6 Å/s by changing the VHF power for different flow rates. Figures 18 and 19 show the FF of a-SiGe alloy middle cells on SS and on BR, respectively, as a function of H_2 flow rate. For all of the cells, the active gas flow rates and other conditions were kept the same. Although the fill factors of the a-SiG alloy cells on SS are largely independent of the H_2 flow rate as indicated in Fig. 18, the values of the cells on BR decrease with the increase of H_2 flow rate when H_2 flow rate is over 130 sccm. Below this value, the fill factor does not depend on the H_2 flow rate. The different behavior observed for the cells on SS and BR may be due to the roughness of the substrates. Microcrystallization may occur more easily on rough surfaces than on smooth surfaces. This point has been observed by the deposition of polycrystalline diamond films. Therefore, we speculate that the cells made on BR with H_2 flow rates higher than 130 sccm contain some microcystallites. The cells on SS do not show the microcrystalline features.

There would not be microcrystalline formation for the conditions mentioned above if the deposition were made with RF excitation. It has been reported that the threshold of H_2 dilution for microcrystallization is much lower in VHF deposition than in RF deposition (Platz et al. 1988). From the current experiments, we learned that we may need to reduce H_2 dilution level when we make a-Si and a-SiGe alloy solar cells with MVHF. Since the threshold of H_2 dilution depends on other deposition conditions such as pressure, VHF power and substrate temperature, for a certain deposition regime, we need to figure out the appropriate H_2 dilution level experimentally.

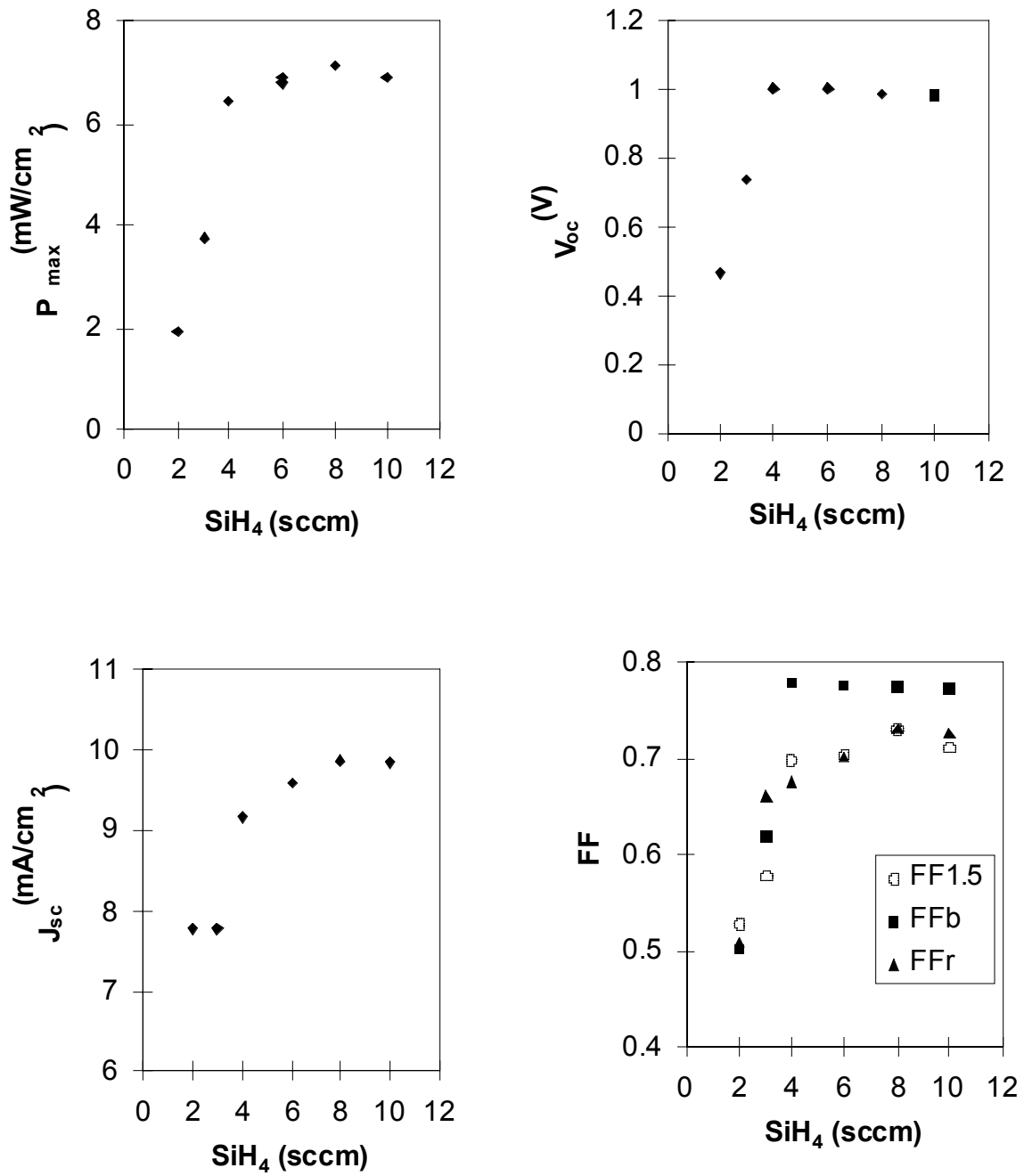**Figure 17.   Characteristic parameters for a-Si alloy solar cells made at different SiH₄ flow rates. The cells were on SS with designed 2100 Å.**
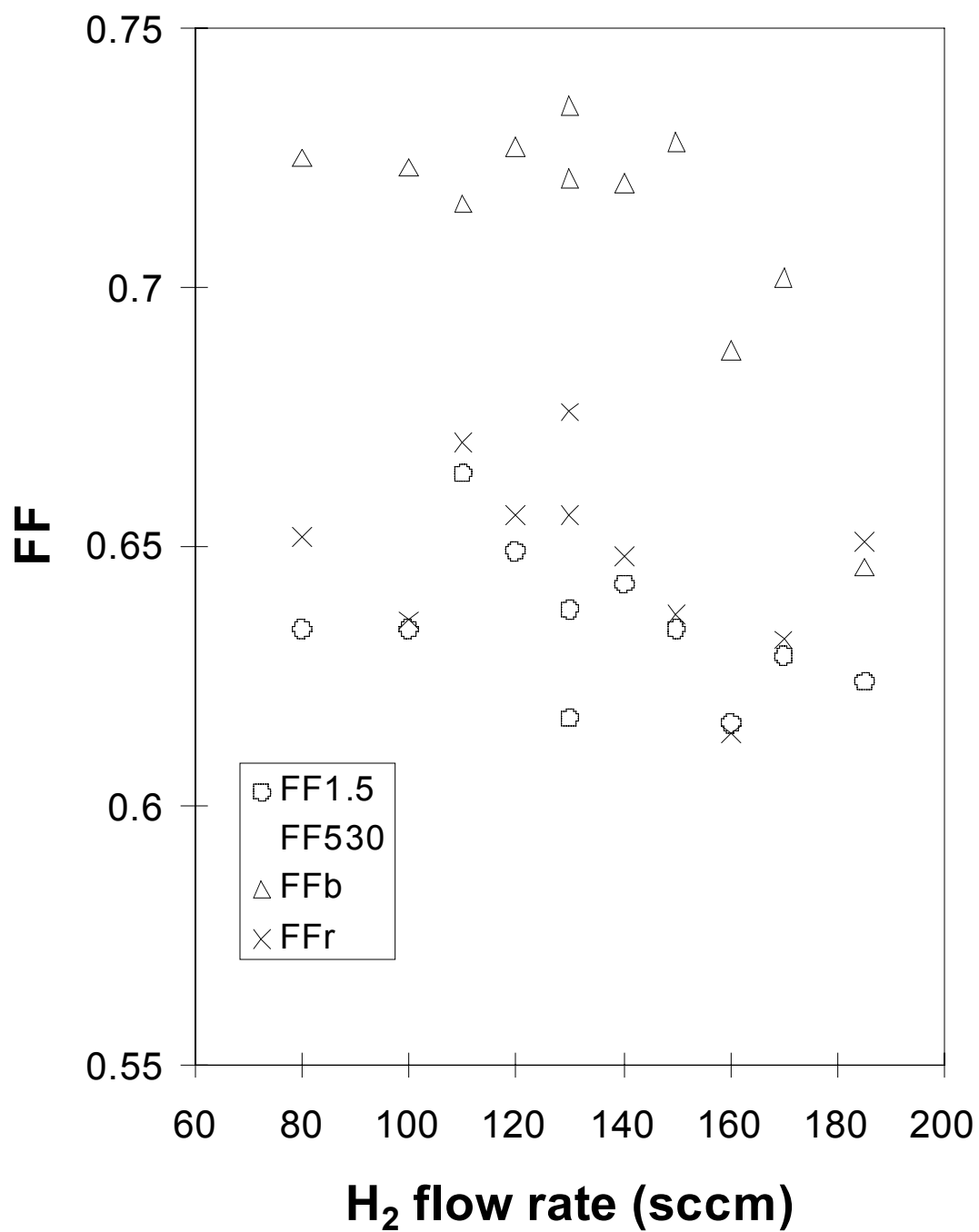
Figure 18. Fill factors of a-SiGe alloy solar cells on SS as a function of H$_2$ flow rate. The cells were made at about 6 Å/s.
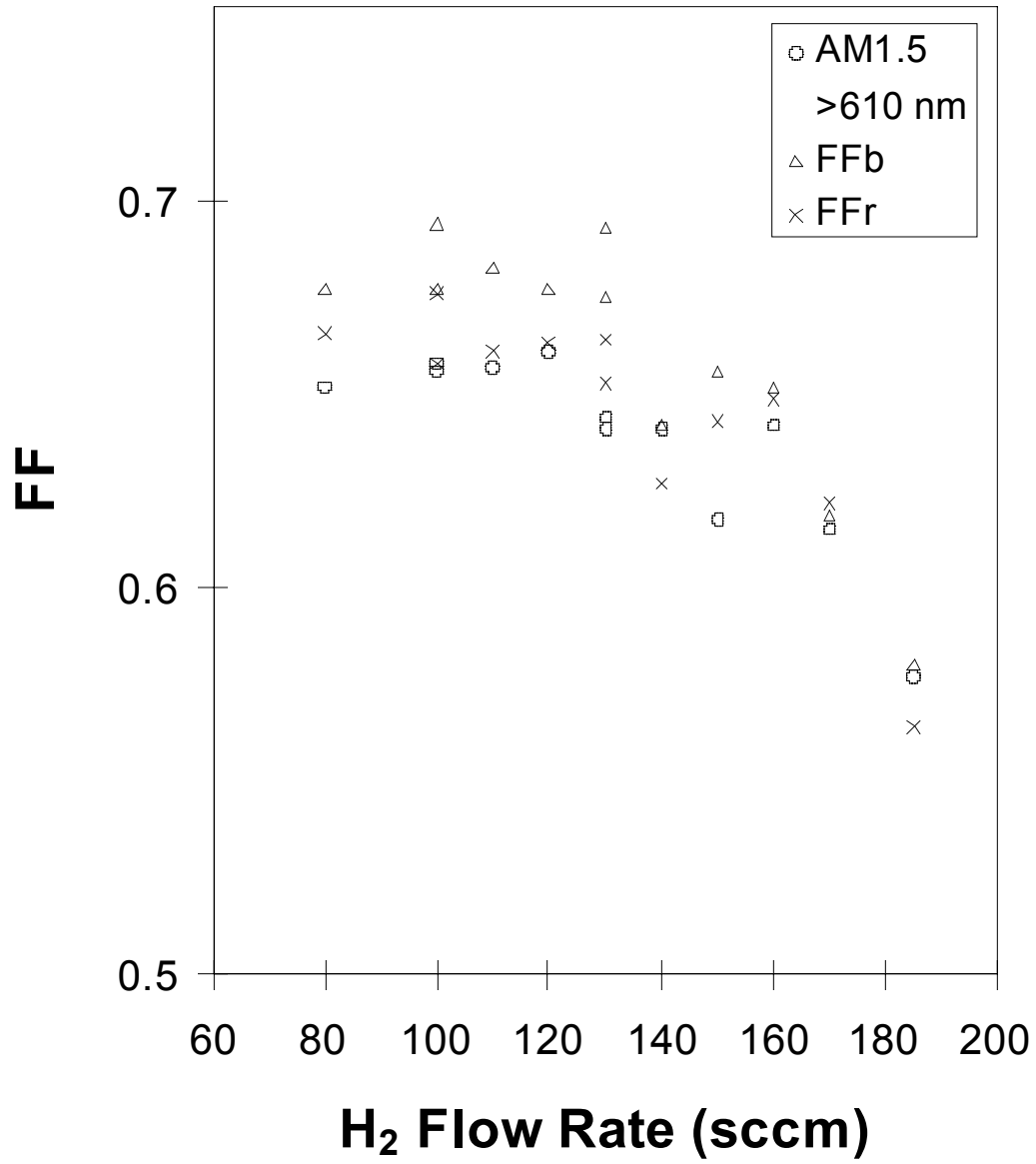
Figure 19. Fill factors of a-SiGe alloy solar cells on BR as a function of H₂ flow rate. The deposition conditions were the same as Fig.18.

Comparison of the stability of RF and MVHF a-Si alloy solar cells

Top, middle and bottom component cells were fabricated in three small area deposition systems. The experiments were conducted to compare the stability of cells deposited with RF and MVHF plasmas. The three systems include the Line (~1 Å/s RF), B (~3 Å/s RF) and VHF (~6 Å/s MVHF). The initial and stabilized J-V characteristics of RF solar cells deposited at 1 and 3 Å/s, and MVHF cells deposited at ~6 Å/s were compared. The middle and bottom cells were deposited without band gap profiling to compare similar cells. State-of-the-art middle and bottom RF cells deposited with band-gap profiling at ~1 Å/s were also compared.

The initial and stabilized active area characteristics of a-Si alloy top cells deposited on stainless steel substrates are listed in Table 6. As reported earlier, the initial characteristic of the a-Si alloy top cells is highest for RF at 1 Å/s. The initial characteristics of the 3 Å/s RF cell is higher than the 6 Å/s MVHF cell, however the stabilized characteristics of the 3 Å/s RF and the 6 Å/s VHF cells are similar.

Table 6. Initial and Stabilized Characteristics of Top Component Cells on Stainless Steel.

Sample	Status	J_{sc} (mA/cm^2)	V_{oc} (V)	FF	Efficiency (%) Active	Total	Deg Rate (%)	Comment
L9654	Initial	8.65	1.016	0.771	6.78	6.31		RF ~1 Å/s
	Stable	8.20	0.965	0.711	5.63	5.24	17	
B3467	Initial	8.74	0.962	0.750	6.31	5.87		RF ~3 Å/s
	Stable	8.41	0.905	0.656	4.99	4.64	21	
VHF6960	Initial	8.66	0.997	0.691	5.97	5.55		MVHF ~6 Å/s
	Stable	8.22	0.955	0.664	5.21	4.85	13	

The J-V characteristics of the a-SiGe alloy middle cells deposited on stainless steel and illuminated with a $\lambda > 530$ nm cut-on filter are listed in Table 7. The RF cells deposited at ~1 Å/s exhibit the highest initial and stabilized P_{max}. The use of band-gap profiling results in a 16% increase in the initial P_{max}. However, both low deposition rate cells with and without bandgap profiling degraded by 20% yielding a 16% higher stabilized P_{max} for the profiled cell. The initial characteristics of the 3 Å/s RF and 6 Å/s MVHF cells are similar, and both cells exhibited similar degradation yielding similar stabilized P_{max}.

Table 7. Initial and Stabilized Characteristics of Middle Component Cells on Stainless Steel.

Sample	Condition	J_{sc} (mA/cm^2)	V_{oc} (V)	FF	P_{max} (mW/cm^2) Active	Total	Deg Rate (%)	Comment
L10524	Initial	9.53	0.759	0.702	5.08	4.72		Profiled RF ~1 Å/s
	Stable	9.06	0.725	0.616	4.05	3.77	20	
L10547	Initial	8.66	0.751	0.656	4.27	3.97		No profile RF ~1 Å/s
	Stable	8.33	0.723	0.566	3.41	3.17	20	
B4576	Initial	7.47	0.764	0.672	3.84	3.57		No profile RF ~3 Å/s
	Stable	7.05	0.723	0.552	2.81	2.61	27	
VHF7797	Initial	7.90	0.766	0.650	3.93	3.65		No profile MVHF ~6 Å/s
	Stable	7.48	0.718	0.548	2.94	2.73	25	

The initial and stabilized characteristics of a-SiGe alloy bottom cells deposited on AgZnO back reflectors are listed in Table 8. Again, the 1Å/s RF cells exhibit the highest initial and stabilized P_{max}. The degradation in the bottom cells with or without bandgap profiling is similar. The effect of band gap profiling is to increase the initial and stabilized P_{max} by 16%. The RF cells deposited at 1 and 3 Å/s exhibit similar degradation. However, the 6 Å/s MVHF bottom cell exhibited the most degradation. Optimization of the MVHF bottom cell is currently underway in an attempt to decrease the degradation to the level of the RF cells.

Table 8. Initial and Stabilized Characteristics of Bottom Component Cells on Back Reflector.

Sample	Condition	J_{sc} (mA/cm2)	V_{oc} (V)	FF	P_{max} (mW/cm^2) Active	Total	Deg Rate (%)	Comment
L10650	Initial	11.72	0.586	0.641	4.40	4.09		Profiled
	Stable	11.43	0.564	0.587	3.78	3.52	14	RF ~1 Å/s
L10655	Initial	9.78	0.620	0.631	3.83	3.56		No profile
	Stable	9.38	0.594	0.578	3.22	2.99	16	RF ~1 Å/s
B4556	Initial	10.27	0.610	0.583	3.65	3.39		No profile
	Stable	9.84	0.583	0.552	3.17	2.95	13	RF ~3Å/s
VHF7902	Initial	9.20	0.624	0.600	3.44	3.20		No profile
	Stable	8.77	0.597	0.535	2.80	2.60	19	MVHF ~6 Å/s

Section 4

Status of Amorphous Silicon Alloy Component and Multi-junction Cells and Modules Deposited in a Large-Area Reactor

Introduction

A prerequisite to fabricating high efficiency modules of aperture area 460-920cm^2 is to optimize the performance and the uniformity of smaller area mini-modules and cells using identical materials and processes. This approach enables the diagnosis and analysis of the devices at both the cell and module levels. Evaluation of the small-area (total area = 0.268cm^2, active area = 0.25cm^2) cells using I-V and Q measurements provide information about the basic device efficiency without the complications of electrical and optical losses associated with modules. It also gives a peek into the device at the component cell level. The analysis of the performance and uniformity of the mini-modules provides a preview of the module efficiency that can be expected from a ~900cm^2 module taking into consideration all the losses related to modules, uniformity, and encapsulation.

Device Fabrication and Measurement

A large-area stainless steel substrate is first sputter-coated with a textured Ag/ZnO back reflector layer. The deposition is over an area of ~1 sq. ft. This is followed by the deposition over the same area of a triple-junction triple-bandgap a-Si/a-SiGe/a-SiGe alloy cell in the 2B machine using conventional glow discharge technique. The top transparent conducting oxide (TCO) is deposited in two different configurations as follows:

Small-area (0. 268cm^2) Devices

This process allows the complete and in depth evaluation of the component cells and light soaking characteristics of both the component and triple-junction cells. In this method, the completed large-area device is cut into 2"x2" substrates. The TCO is deposited through an evaporation mask to yield devices of total area 0.268cm^2. These devices are used for I-V and Q measurements. Stable cell results are obtained by exposing several of the representative 2"x2" samples obtained from the original 900cm^2 substrate.

Module and Mini-module Fabrication

This process allows the fabrication of modules and mini-modules. The TCO film is deposited over the entire area. The TCO film is then etched in two different ways: (1) to fabricate a module of aperture area 450cm^2 and (2) to demarcate an array of nine 3"x3" cells spread over an area of 9"x9". The aperture area of each of the 3"x3" devices is 40-45cm^2. One of the 3"x3" sections also has an ITO-etched 5x5 array of 0.268cm^2 devices. The 0.268cm^2 devices are used for the small-area I-V and Q measurements. A dc-source ORC solar simulator is used for the I-V measurements.

The module and mini-module fabrication process is now summarized. The 450cm^2 aperture area substrate for module fabrication and the eight 40-45cm^2 aperture area substrates for mini-module are processed in a similar way. Front surface grids are applied using a wire bonding process and bus bars are connected. The bare modules/mini-modules are measured in a Spire pulsed solar simulator Model

240A equipped with a peak detector circuit board. The modules/mini-modules are then encapsulated using a stack of Tefzel and EVA. Another set of I-V measurements is made on the encapsulated modules/mini-modules under the Spire solar simulator.

The I-V and Q measurements of the $0.25cm^2$ small-area cells can be used to characterize the mini-modules since all the deposition steps are identical. This approach eliminates any ambiguity related to the comparison of results of the small-area cells and the mini-modules. Further, all the processing steps, the materials used, and the measurement conditions are identical to the ones used for fabricating the large-area $460cm^2$ or $900cm^2$ modules. The only difference is that the ITO etch pattern is different (of larger area) for the large-area modules compared to the case of the mini-modules. Therefore, the error involved in extrapolating the results of the mini-modules to the large-area modules is minimized.

Stability Studies

Two kinds of samples were used for the stability studies. The first were the small-area ($0.268cm^2$) component and triple-junction cells and the second were the modules/mini-modules. For the small-area cells, several 2"x2" substrates encompassing several unencapsulated $0.268cm^2$ total area devices were first measured. The average efficiency was obtained on each substrate. The average efficiency of all the substrates gives an estimate of the expected initial module efficiency. Only encapsulated modules/mini-modules were used for the light soaking. The light soaking for all samples was done under one-sun, 50^0C, and open-circuit conditions.

Results of Component Cells

Top Cell on Stainless Steel Substrate

The a-Si alloy top cell (of a triple-junction device) was deposited on a large area stainless steel substrate with no back reflector. Small-area cell performance was measured on six 2"x2" substrates, representing the large-area substrate. The average efficiency was measured as a function of exposure time. The average stabilized efficiency of all the substrates after 1000 hours of light soaking can be extrapolated to obtain the stable module efficiency. The final results of six 2"x2" substrates of 2B5735 are tabulated in Table 9. Each data point in the table is an average of several $0.268cm^2$ total area devices on that substrate. The average values of all the six substrates are given at the bottom of the table. These average values can be considered to be representative of the entire large-area 12"x12" substrate. The overall initial average efficiency is 5.9% and the stabilized value is 5.4%. The stabilized value of 5.4% meets the Phase I milestone of 5.0% for the first year of the program.

Table 9. Average Results of Small-Area a-Si Alloy Top Cells on a 2"x2" Stainless Steel Substrate.

Sample 2B5735	Active area (cm^2)	Total area (cm^2)	Light Soak (Hours)	J_{sc} (mA/cm^2)	V_{oc} (V)	FF	Efficiency (%) Active area	Efficiency (%) Total area
LD5	0.25	0.268	0	9.12	0.988	0.727	6.6	6.1
			1031	9.00	0.941	0.697	5.9	5.5
LH4	0.25	0.268	0	8.75	0.981	0.722	6.2	5.8
			1031	8.56	0.936	0.704	5.6	5.3
LG1	0.25	0.268	0	8.67	0.974	0.724	6.1	5.7
			1031	8.60	0.933	0.695	5.6	5.2
LH6	0.25	0.268	0	8.86	0.981	0.725	6.3	5.9
			1031	8.67	0.940	0.698	5.7	5.3
LC1	0.25	0.268	0	9.23	0.990	0.724	6.6	6.2
			1031	9.15	0.946	0.689	6.0	5.6
LF2	0.25	0.265	0	9.02	0.986	0.711	6.3	5.9
			1031	8.79	0.940	0.688	5.7	5.3
Average	**0.25**	**0.268**	**0**	**8.94**	**0.983**	**0.722**	**6.4**	**5.9**
			1031	**8.80**	**0.939**	**0.695**	**5.7**	**5.4**
Phase I milestone		*1.0*	*1000*					*5.0*

Middle Cell on Stainless Steel Substrate

A similar work has been done on middle cell on stainless steel substrate. Six representative 2"x1" pieces with 0.268cm^2 total-area devices were prepared. The initial performance of the devices was measured under AM1.5 illumination using a $\lambda > 530$nm cut-on filter. The devices were then light soaked under open circuit, one sun with filter, and 50^{0}C conditions. The filter was selected such that the intensity corresponded to a J_{SC} of ~8-9mA/cm^2. The initial and 1072 hours light soaked results of the six substrates are summarized in Table 10. Each value in the table represents the average of several 0.268cm^2 devices on that substrate. The average stable values of p_{max} at $\lambda > 530$nm for the six substrates are in the range of 3.36-3.68mW/cm^2. The average for all the substrates shown at the bottom of Table 10 is 3.6mW/cm^2 and is representative of the entire large-area 12"x12" substrate. The stabilized value of 3.6mW/cm^2 meets the Phase I milestone of 3.1 mW/cm^2 for the first year of the program.

Table 10. Average Results of Small-area a-SiGe Alloy Middle Cells on a 2"x2" Stainless Steel Substrate.

Sample 2B5905	Active area (cm^2)	Total area (cm^2)	Light Soak (Hours)	J_{sc} (mA/cm^2)	V_{oc} (V)	FF	P_{max}>530nm (mW/cm^2) Active area	Total area
LA2	0.25	0.268	0	9.78	0.725	0.684	4.84	4.51
			1072	9.59	0.685	0.599	3.92	3.66
LA4	0.25	0.268	0	9.57	0.732	0.671	4.70	4.38
			1072	9.55	0.687	0.583	3.83	3.57
LC1	0.25	0.268	0	9.73	0.728	0.682	4.83	4.51
			1072	9.50	0.688	0.593	3.89	3.63
LE	0.25	0.268	0	9.23	0.742	0.671	4.60	4.29
			1072	9.02	0.700	0.571	3.60	3.36
LH2	0.25	0.268	0	9.24	0.733	0.657	4.45	4.15
			1072	9.23	0.692	0.576	3.70	3.45
LI	0.25	0.265	0	9.45	0.724	0.692	4.72	4.40
			1072	9.42	0.685	0.610	3.94	3.68
Average	**0.25**	**0.268**	**0**	**9.50**	**0.730**	**0.676**	**4.7**	**4.4**
			1072	**9.38**	**0.689**	**0.589**	**3.8**	**3.6**
Phase I milestone		*1.0*	*1000*					*3.1*

Bottom Cell on Ag/ZnO Substrate

For the bottom cell, a Ag/ZnO back reflector substrate has been used. Six representative 2"x2" pieces with 0.268cm^2 total-area devices were prepared. The initial performance of the devices was measured under AM1.5 illumination using a λ>630nm cut-on filter. The devices were then light soaked under open circuit, one sun with filter, and 50^{0}C conditions. The filter was selected such that the intensity corresponded to a J_{SC} of 8.5-9.5mA/cm^2. The initial and 621 hour light soak results of the six substrates are summarized in Table 11. Each value in the table represents the average of several 0.268cm^2 devices on that substrate. The average stable values of p_{max} at λ>630nm for the six substrates are in the range of 3.08-3.30mW/cm^2. The average for all the substrates shown at the bottom of Table 11 is 3.2mW/cm^2 and is representative of the large-area 12"x12" substrate. The stabilized value of 3.2 meets the Phase I milestone of 3.lmW/cm^2 for the first year of the program.

Table 11. Average Results of Small-area a-SiGe Alloy Bottom Cells on a 2"x2" Ag/ZnO Substrate.

Sample 2B6172	Active area (cm^2)	Total area (cm^2)	Light Soak (Hours)	J_{sc} (mA/cm^2)	V_{oc} (V)	FF	P_{max}>630nm (mW/cm^2) Active area	Total area
LA2	0.25	0.268	0	11.49	0.596	0.606	4.15	3.85
			621	10.87	0.571	0.559	3.47	3.23
LI	0.25	0.268	0	11.49	0.594	0.626	4.27	3.97
			621	10.87	0.570	0.547	3.39	3.15
LC1	0.25	0.268	0	11.49	0.601	0.582	4.01	3.74
			621	10.87	0.577	0.528	3.31	3.08
LB5	0.25	0.268	0	11.49	0.596	0.596	4.08	3.80
			621	10.87	0.577	0.534	3.34	3.11
LD6	0.25	0.268	0	11.49	0.591	0.592	4.02	3.73
			621	10.87	0.572	0.556	3.46	3.22
LF2	0.25	0.265	0	11.49	0.596	0.615	4.21	3.92
			621	10.87	0.577	0.566	3.55	3.30
Average	**0.25**	**0.268**	**0**	**11.49**	**0.596**	**0.603**	**4.1**	**3.8**
			621	**10.87**	**0.574**	**0.548**	**3.4**	**3.2**
Phase I milestone		***1.0***	***1000***					***3.1***

Results of Triple-Junction Cells

Triple-junction triple-bandgap a-Si/a-SiGe/a-SiGe alloy cells were deposited on Ag/ZnO back reflector. The top, middle, and bottom components of the triple-junction structure were similar to the corresponding devices described in the preceeding section. Each component cell incorporated high hydrogen dilution in order to obtain the best results. The thickness and the bandgap of each cell were optimized to obtain the highest mutijunction device efficiency. Small-area cell performance was measured on four 2"x2" substrates, representing the large-area substrate. The initial and the stabilized results after 1067 hours of light soak are shown in Table 12.

Table 12. Average Results of Small-Area Triple-Junction Cells on 2"x2" Ag/ZnO Back Reflector.

Sample 2B5735	Active area (cm^2)	Total area (cm^2)	Light Soak (Hours)	J_{sc} (mA/cm^2)	V_{oc} (V)	FF	Efficiency (%) Active area	Total area
LE	0.25	0.268	0	8.84	2.281	0.708	14.3	13.3
			1067	8.64	2.209	0.660	12.6	11.7
LF4	0.25	0.268	0	8.77	2.279	0.717	14.3	13.4
			1067	8.49	2.208	0.664	12.5	11.6
LD4	0.25	0.268	0	8.81	2.280	0.713	14.3	13.4
			1067	8.43	2.207	0.666	12.4	11.6
LC1	0.25	0.268	0	8.77	2.250	0.718	14.2	13.2
			1067	8.49	2.178	0.674	12.5	11.6
Average	**0.25**	**0.268**	**0**	**8.80**	**2.273**	**0.714**	**14.3**	**13.3**
			1067	**8.51**	**2.201**	**0.666**	**12.5**	**11.6**
Phase I milestone		***1.0***	***1000***					***11.2***

The four substrates are numbered LE, LF4, LD4, and LC1. Each value in the table represents the average of several 0.268cm^2 devices on that substrate. The overall average values of initial efficiency of all the substrates are active-area efficiency = 14.3% and total-area efficiency = 13.3%, respectively. The corresponding values for the 1067 hours light stabilized case are 12.5% and 11.6%, respectively, and is representative of the large-area 12"x12" substrate. The Phase I milestone shown in the same table for the stabilized total-area efficiency = 11.2%. The stabilized total-area efficiency of 11.6% meets the Phase I milestone.

The initial J-V characteristics of the best cell on substrate 2B5616LD4 are shown in Fig. 20. The corresponding initial Q of the component cells and the total integrated Q of the device are shown in Fig. 21. The measurements show that for the 0.25cm^2 active area (0.268cm^2 total area) device, the V_{OC} = 2.280V, J_{SC} (from Q) = 8.8lmA/cm^2, FF = 0.721, and active area efficiency ~14.5%. The current of the top, middle, bottom cells, and the complete device are 8.92, 8.86, 8.81, and 26.59mA/cm^2, respectively. The stabilized J-V characteristics of the best device and the Q measurements after the light soak are shown in Fig. 22 and 23, respectively. The stabilized results are V_{OC} = 2.213V, J_{SC} (from Q) = 8.79mA/cm^2, FF = 0.661, and active area efficiency ~12.9%. The current of the top, middle, bottom, and the complete device are 8.87, 8.79, 8.82, and 26.48mA/cm^2. The stabilized efficiency of 12.9% is close to the world-record value of 13.0% reported earlier by us from the small-area LINE machine.

Figure 20. Initial J-V characteristic of a triple-junction device of efficiency 14.5%.
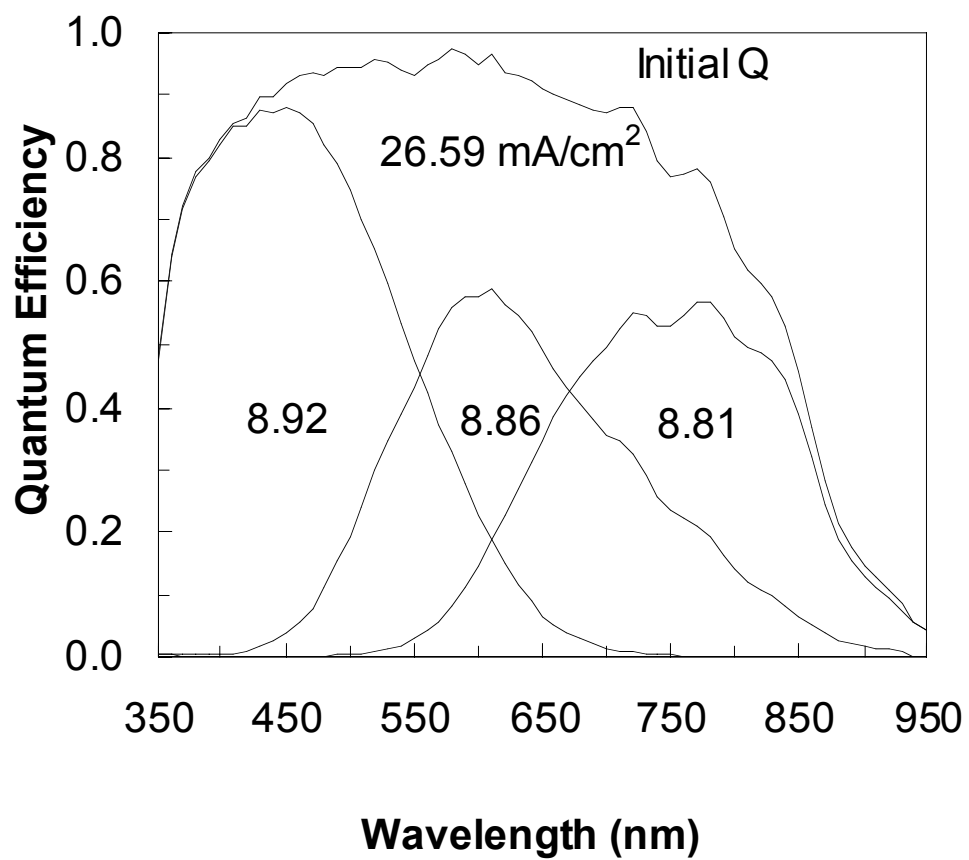
Figure 21. Initial Q characteristic of the cell shown in Fig. 20.

2B5616LD4 Final

Active area = 0.25 cm ^{2}
V_{oc} = 2.213 V
J_{sc} (Q) = 8.79 mA/cm ^{2}
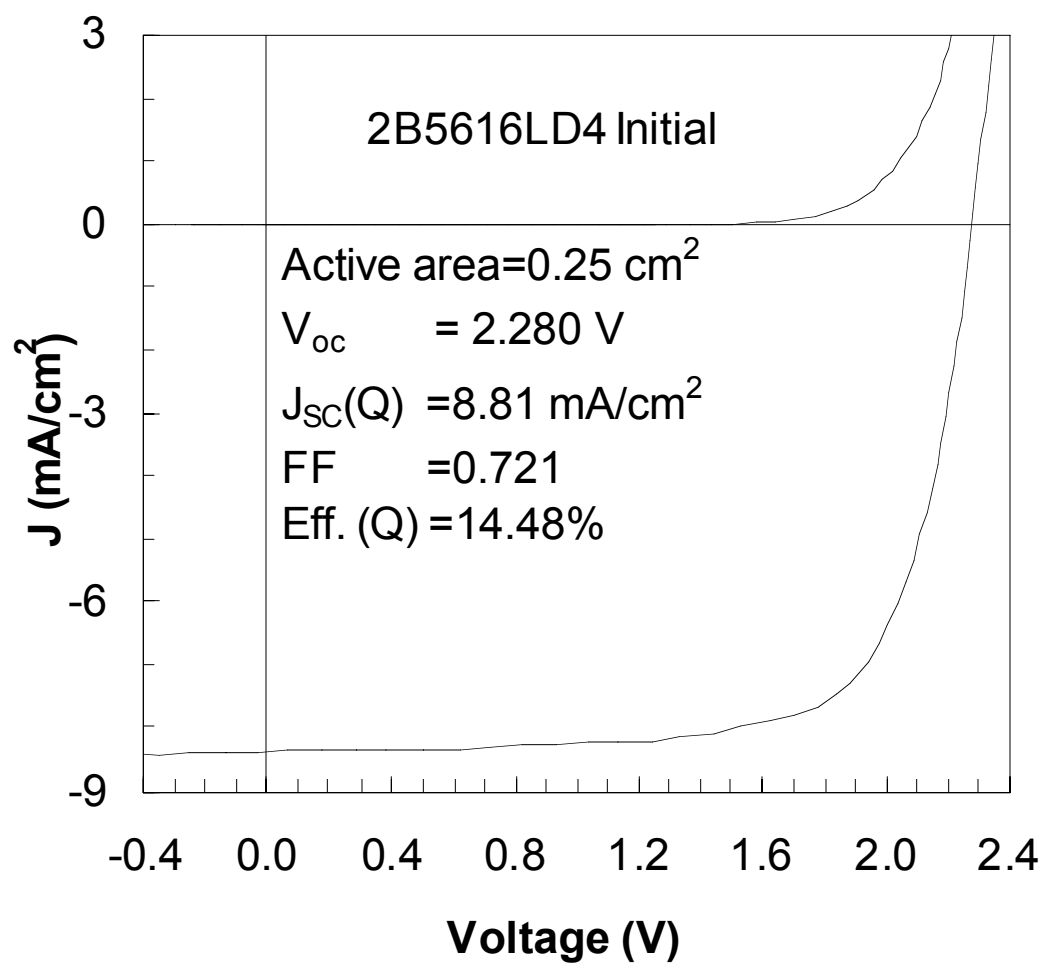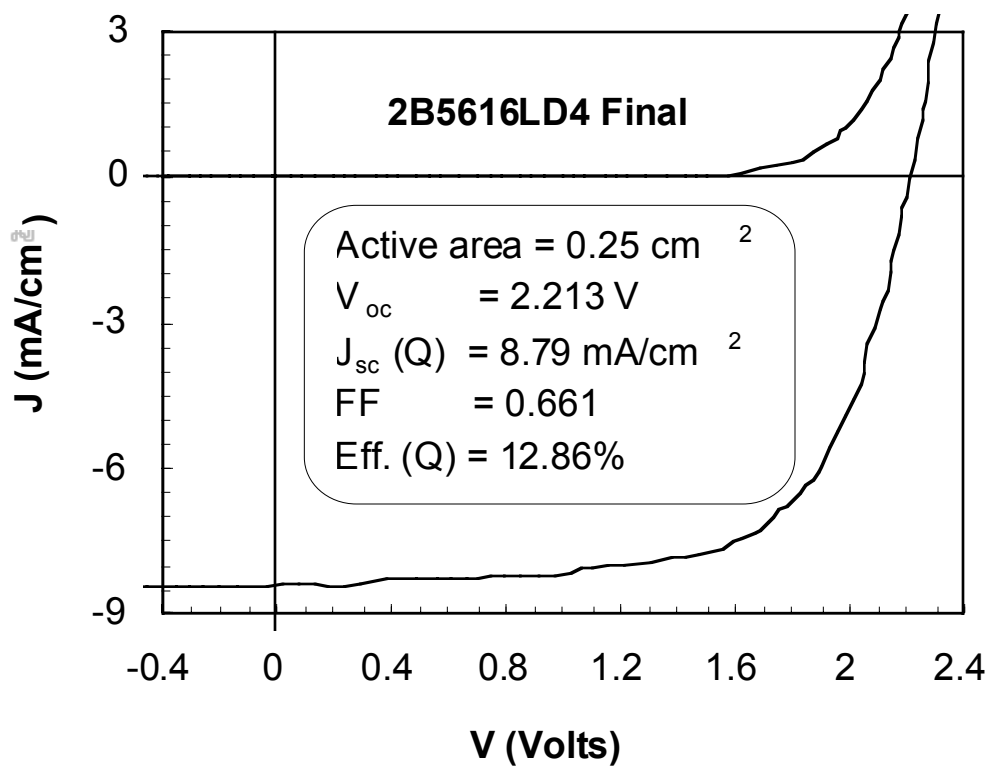FF = 0.661
Eff. (Q) = 12.86%

Figure 22. Stable J-V characteristic of a triple-junction device of efficiency 12.9%.
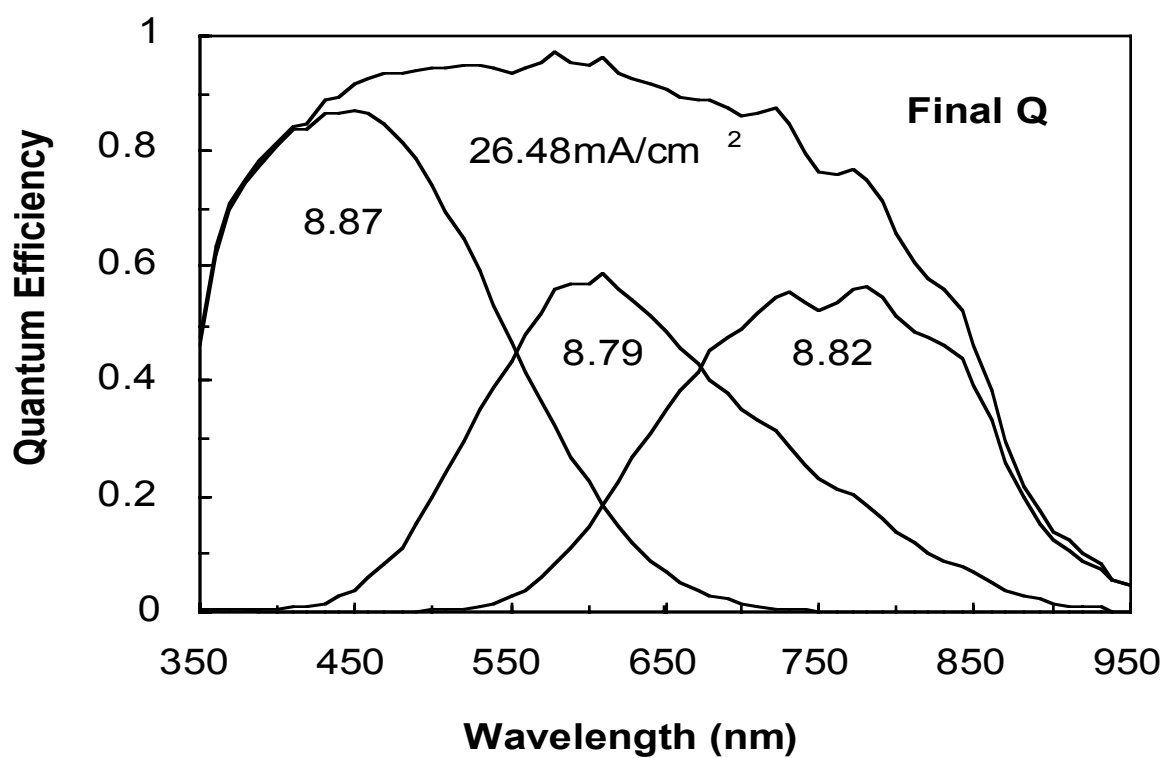
Figure 23. Stable Q characteristic of the cell shown in Fig. 22.

Module Results

The module fabrication process has been briefly described above. Three kinds of modules have been fabricated corresponding to the three aperture areas: (1) 40-45cm^2, (2) 460cm^2, and (3) 900cm^2. All I-V measurements have been made using a Spire pulsed solar simulator equipped with a peak detector circuit board. The initial and stable results of the various modules are described.

Mini-modules of Aperture Area 40-45cm^2

The initial I-V results of the mini-modules for two different runs made in the 2B machine, 5549 and 5552, are summarized in Table 13. The measurements have been made on the bare unencapsulated mini-modules. The entry under the column "Sample #" refers to the different 3"x3" sections of each run. The aperture area in each case is 44.39cm^2. The values of initial efficiency for the different samples of 2B 5549 and 5552 are 12.7-13.3% and 12.5-13.1%, respectively. The average efficiencies for the two cases are 13.0 and 12.8%, respectively. The uniformity over the 9"x9" area spanned by the results shown in the table is good. The spread in efficiency is ±2.5% of the average efficiency in both cases.

As shown in Table 13, the highest initial efficiency of 13.3% has been obtained on 2B 5549#E1. The I-V characteristics of this mini-module are shown in Fig. 24. The V_{OC} = 2.30V, I_{SC} = 364mA, FF = 0.705, and P_{max} = 590mW. This is the highest efficiency obtained on any module made in the 2B machine.

Table 13. Summary of Initial I-V Characteristics of Two Sets of Bare Mini-Modules.

2B #	Sample #	Aperture Area (cm^2)	V_{OC} (V)	I_{SC} (mA)	FF	P_{max} (mW)	Efficiency (%)
5549	El	44.39	2.30	364	0.705	590	13.3
	E2	44.39	2.30	371	0.687	586	13.2
	E3	44.39	2.30	371	0.673	575	12.9
	G1	44.39	2.29	358	0.699	572	12.9
	G3	44.39	2.31	365	0.671	565	12.7
	Average	**44.39**	**2.30**	**366**	**0.687**	**578**	**13.0**
5552	El	44.39	2.27	366	0.691	574	12.9
	E2	44.39	2.29	368	0.690	582	13.1
	E3	44.39	2.29	364	0.676	563	12.7
	Fl	44.39	2.25	359	0.703	568	12.8
	G1	44.39	2.25	357	0.691	555	12.5
	G2	44.39	2.28	363	0.695	575	13.0
	G3	44.39	2.30	366	0.681	575	12.9
	Average	**44.39**	**2.28**	**363**	**0.690**	**570**	**12.8**

2B5549E1 Initial

Aperture area = 44.39cm^2
V_{oc} = 2.30V
I_{sc} = 0.364A
FF = 0.705
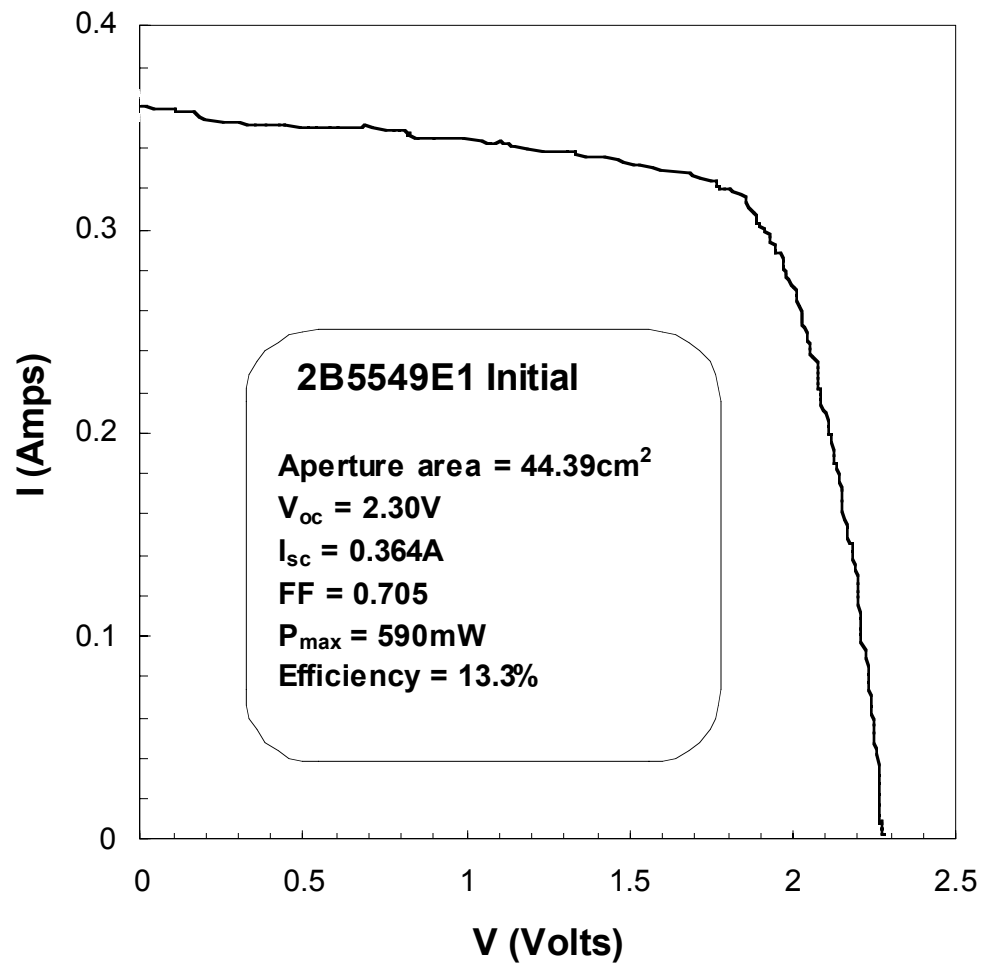P_{max} = 590mW
Efficiency = 13.3%

Figure 24. Initial I-V characteristic of a bare mini-module of aperture area 44.39cm^2.

Table 14. Summary of Initial I-V Characteristics of Encapsulated Mini-Modules.

2B #	Sample #	Aperture Area (cm^2)	V_{OC} (V)	I_{SC} (mA)	FF	P_{max} (mW)	Efficiency (%)
5549	E2L	41.28	2.28	321	0.710	519	12.6
	E3L	41.28	2.28	325	0.686	509	12.3
	GIL	41.28	2.25	317	0.696	497	12.0
	Average	**41.28**	**2.27**	**321**	**0.697**	**508**	**12.3**
5552	ElL	41.28	2.24	320	0.700	502	12.2
	F1L	41.28	2.23	320	0.695	496	12.0
	G2L	41.28	2.25	320	0.707	509	12.3
	G3L	41.28	2.29	322	0.697	514	12.4
	Average	**41.28**	**2.25**	**321**	**0.700**	**505**	**12.2**

Some of the high efficiency mini-modules shown in Table 13 have been encapsulated. The initial results are summarized in Table 14. The aperture area of the mini-modules is 41.28cm^2. The average efficiency of three samples of run 2B 5549 is 12.3% and the average of four samples of run 2B 5552 is 12.2%. The highest efficiency of 12.6% is obtained on 2B 5549#E2L. The values of V_{OC} = 2.28V, I_{SC} = 321mA, FF = 0.710, and Pmax = 519mW. This is the highest efficiency obtained on any module made in the 2B machine.

Four of the encapsulated mini-modules were light soaked. The initial and stable values after 1056 hours of light soak are summarized in Table 15. The initial efficiency is in the range of 12.1-12.6%. The stable aperture area efficiency is 10.9-11.2%. These values project the efficiency of larger area modules since the design and fabrication procedures are identical. Module 5549#E2L exhibits the highest stable efficiency of 11.2%. The I-V characteristics of this module are shown in Fig. 25. The aperture area is 41.2cm^2, V_{OC} = 2.21V, I_{SC} = 317mA, FF = 0.655, and P_{max} = 460mW. This is the highest stabilized aperture-area efficiency obtained on a fully encapsulated module.

Table 15. Spire Results of Light Soak of Four Mini-Modules.

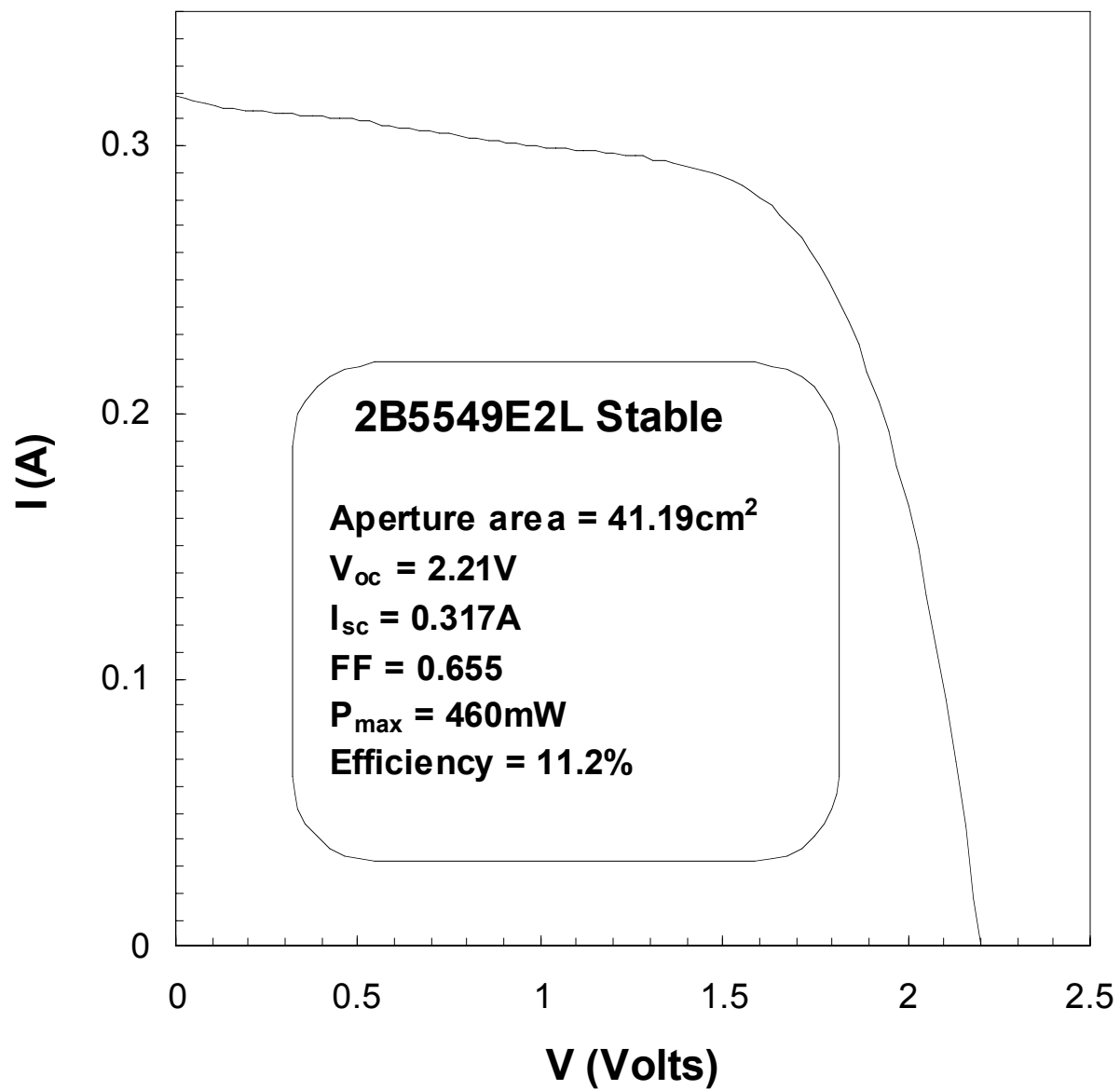| 2B #	Sample #	Aperture Area (cm^2)	Light exposure (Hours)	V_{OC} (V)	I_{SC} (mA)	FF	P_{max} (mW)	Efficiency (%)
5546	F2L	41.30	0	2.26	319	0.693	501	12.1
			1056	2.20	313	0.656	453	11.0
5549	E2L	41.19	0	2.28	321	0.710	519	12.6
			1056	2.21	317	0.655	460	11.2
5549	E3L	41.54	0	2.28	325	0.686	509	12.3
			1056	2.22	319	0.642	455	10.9
5552	ElL	41.41	0	2.24	320	0.700	502	12.2
			1056	2.19	317	0.656	454	11.0

2B5549E2L Stable

Aperture area = 41.19cm^2
V_{oc} = 2.21V
I_{sc} = 0.317A
FF = 0.655
P_{max} = 460mW
Efficiency = 11.2%

Figure 25. Stable I-V characteristic of an encapsulated mini-module.

Modules of Aperture Area ~460cm^2

We have fabricated modules of aperture area ~460cm^2. Initial and stable results after 1000 hours of light soak of three encapsulated modules are summarized in Table 16. The initial efficiency of the modules is 12.1-12.3%. Module 2B5632L of aperture area 452.6cm^2 exhibits the highest initial efficiency of ~12.3%; the V_{OC} = 2.30V, I_{SC} = 3.51A, FF = 0.689, and P_{max} = 5.56W. The stabilized efficiency of the modules is 11.0-11.1%. The stabilized results of the highest efficiency module 2B5632L are efficiency = 11.1%, V_{OC} = 2.23V, I_{SC} = 3.46A, FF = 0.652, and P_{max} = 5.02W. This is the highest stable efficiency obtained on an encapsulated module of this size. A graph of efficiency of the three modules as a function of light soak time is shown in Fig. 26. The figure shows that substantial saturation occurs after ~400 hours.

Table 16. Initial and Stable Spire Results of Encapsulated Modules of Aperture Area ~460cm^2.

Module	Aperture area (cm^2)	Light Soak (Hours)	V_{OC} (V)	I_{SC} (A)	FF	P_{max} (W)	Eff (%)
2B5632L	452.62	0	2.30	3.51	0.689	5.56	12.28
		1000	2.23	3.46	0.652	5.02	11.09
2B5645L	450.91	0	2.29	3.46	0.693	5.50	12.20
		1000	2.23	3.40	0.657	4.98	11.04
2B5654L	452.62	0	2.30	3.51	0.679	5.48	12.11
		1000	2.22	3.47	0.644	4.96	10.96

Modules of Aperture Area ~920cm^2

Several encapsulated modules of aperture area 920cm^2 have been fabricated. The results of seven modules are summarized in Table 17. The initial efficiency is in the range of 11.7-12.1%. Module 567577L of aperture area 918.0cm^2 exhibits the highest efficiency of 12.1%; the V_{OC} = 4.60V, I_{SC} = 3.57A, FF = 0.678, and P_{max} = 11.13W. One of the modules, 558485, of initial efficiency 11.5% has been light soaked for 1056 hours. The stabilized values of the module are efficiency = 10.5%, V_{OC} = 4.41V, I_{SC} = 3.42A, FF = 0.637, and P_{max} = 10.83W. This is the highest value of stable efficiency that has been obtained on a module of this area. Note that the initial efficiency of the other modules is higher.
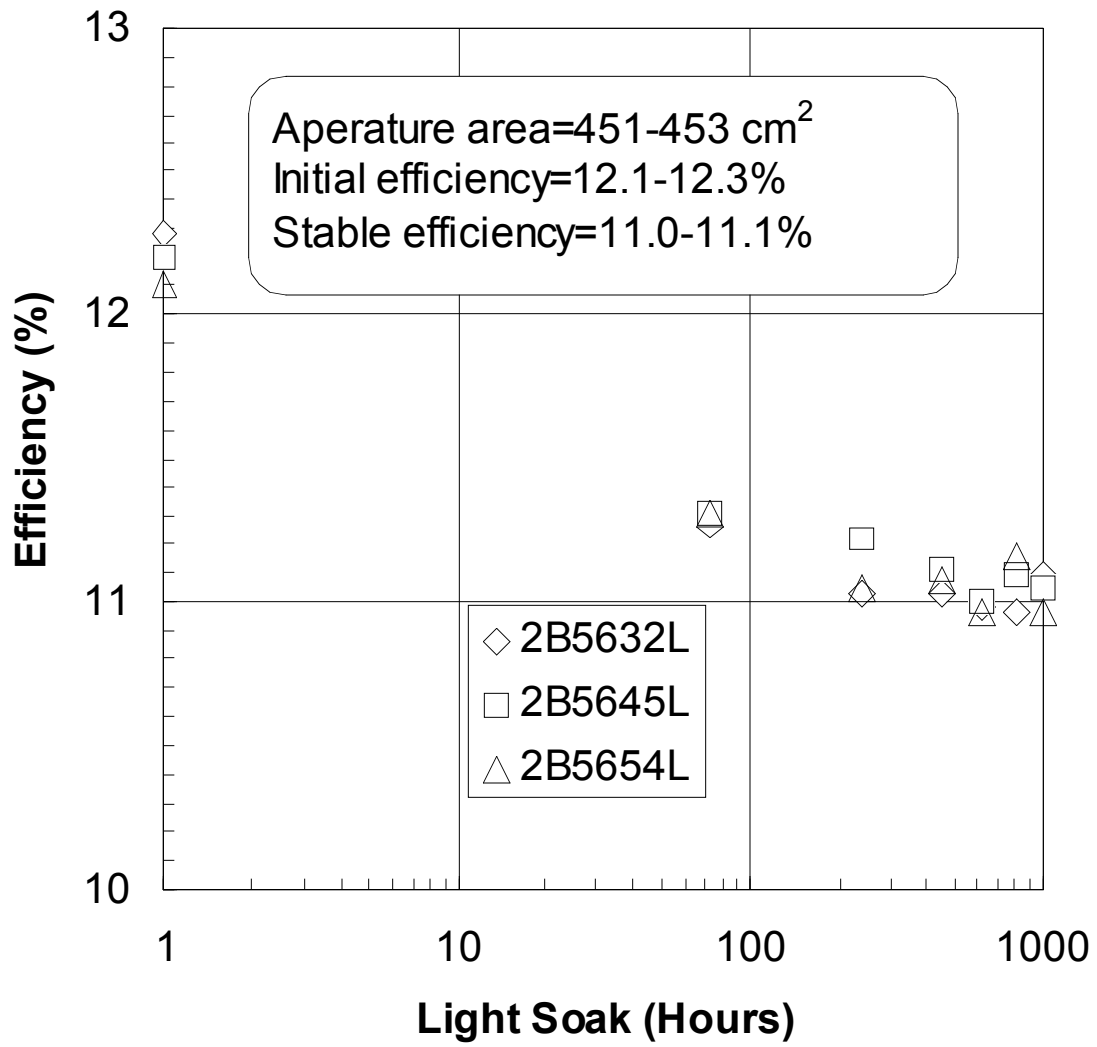
Figure 26. Stability of encapsulated modules of aperture area ~450cm^2.

Table 17. Initial and Stable Spire Results of Encapsulated Modules of Aperture Area ~920cm^2.

Module	Aperture Area (cm^2)	Light Soak (Hours)	V_{OC} (V)	I_{SC} (A)	FF	P_{max} (mW)	Efficiency (%)
562194L	918.2	0	4.56	3.51	0.680	10.88	11.9
563946L	919.3	0	4.58	3.51	0.683	10.95	11.9
565398L	919.9	0	4.57	3.55	0.679	11.02	12.0
566179L	922.1	0	4.56	3.59	0.657	10.75	11.7
566566L	907.1	0	4.57	3.51	0.675	10.53	11.9
567577L	918.0	0	4.60	3.57	0.678	11.13	12.1
558485L	915.4	0	4.55	3.41	0.680	10.55	11.5
		1056	4.41	3.42	0.637	9.60	10.5

NREL Measurement of Modules

Three of the ~920cm^2 modules shown in Table 17, #s 566179L, 566566L, and 567577L, were sent to NREL for confirmation of the I-V measurements. NREL made three types of measurements: (1) indoor using Spire solar simulator model 240A equipped with a peak detector circuit board, (2) indoor using Large Area Continuous Solar Simulator (LACSS), and (3) outdoor using Standard Outdoor Measurement System (SOMS). A summary of the NREL measurements and the corresponding United Solar Spire measurements is provided in Table 18.

All the United Solar Spire measurements were made using the same model solar simulator as the NREL Spire. The table shows that the initial efficiency measured by NREL is lower all across the board. The United Solar efficiency values are 11.7-12.1%; the corresponding NREL numbers are 10.90-11.40%. The NREL efficiency measurements are 4.2-9.9% lower than the United Solar ones. Even the NREL Spire measurements are 5.8-8.3% lower than the United Solar ones. Almost the entire discrepancy can be attributed to the discrepancy in the I_{sc} measurements: 5.7-9.4% between the two Spire measurements and 3.5-7.0% between the United Solar Spire and NREL outdoor values.

In order to understand the discrepancy of especially the Spire measurements at the two places, we have re-evaluated the United Solar Spire solar simulator using other modules and investigated its performance over time. In principle, the two measurement circuits are similar and it is difficult to understand any appreciable discrepancy. The first test was the measurement of a crystal silicon module under the Spire and plot the efficiency as a function of time. Figure 27 shows a plot of the normalized P_{max} of the c-Si module as a function of time from September 1996 to August 1998. The figure shows that over a period of two years ending August 1998, the c-Si module measurements are within ±1.0% of its average. This result shows pretty good consistency of the Spire measurements and also demonstrates that the overall intensity has remained constant.

In order to determine the consistency of the spectrum of the United Solar Spire solar simulator, several modules were remeasured. Table 19 shows the performance of the modules at various times. Wherever possible, the corresponding NREL Spire measurements are also listed. The first three modules, 2B2469F, 2B2438F, and 2B2431F, were first measured at United Solar in November 1993. These were remeasured in September 1998. The new efficiency measurements are 0.4-3.7% higher. A closer look shows that the new fill factor values are lower and is attributed to new higher series resistance of the modules (not shown). It appears that there is some internal contact resistance problem. It is, therefore, better to evaluate only the I_{SC} values. The new values are 2.2-4.9% higher which is much less than the discrepancy shown in Table 19. The last two modules, 2B2452F and 2B2465F, were measured at United Solar in November 1993 and at NREL in December 1993. At that time, the United Solar efficiency values were 4.2-5.5% lower and the I_{SC} values were 7.0-7.1% lower.

Based on the above it is clear that the United Solar Spire solar simulator has been reasonably consistent over the last few years. We, therefore, believe that the United Solar measurements are reliable. However, at present, we have no explanation for the discrepancy between the United Solar and the NREL measurements.

The fourth module in Table 18, 563946L, has been measured at United Solar under the Spire solar simulator and Sandia National Laboratory under outdoor conditions. The efficiency measured at United Solar and Sandia are 12.3% and 11.7%, respectively. This corresponds to a discrepancy of 4.9%. Note that the discrepancy in the I_{sc} is only 1.1%. The Sandia value of V_{oc}, 4.49V, is lower than the corresponding United Solar value of 4.58V which suggests that the measurement temperature at Sandia might be higher than 25^0C. Since the modules exhibit negative temperature coefficient of efficiency, it is conceivable that the Sandia number would be higher than the measured value of 11.7%. Still, the Sandia number is much higher than the highest NREL measured value of 11.21%. Efforts are under way to resolve these discrepancies in measurement at the various laboratories.

New World Record Stable 10.5% Module Efficiency

The first three modules in Table 18 were light soaked at NREL. Figure 28 shows a plot of NREL Spire efficiency as a function of light soak time. Preliminary results show that both the Spire and outdoor-measured stabilized efficiency of the modules are in the range of 10.1-10.5%. A stabilized efficiency of 10.5% corresponds to a new world record for an a-Si alloy module of this size. This achievement also satisfies the Phase I milestone as shown at the bottom of Table 18.

Table 18. Comparison of Module Performance at United Solar, NREL, and Sandia National Lab.

| Module 2B	State	Area (cm^2)	Laboratory	Temp. (^{0}C)	V_{oc} (V)	I_{sc} (A)	FF	Efficiency (%)
566179L	Initial	922.1	United Solar Spire	25	4.56	3.59	0.657	11.7
		915.9	NREL Spire	25.1	4.519	3.2907	0.6753	10.96
			NREL LACSS	29.0	4.422	3.4336	0.6675	11.10
			NREL SOMS @ 964W/m^2	31.7	4.387	3.2179	0.6800	10.90
	Stable		NREL Spire	25.4	4.381	3.2502	0.6491	10.09
			NREL LACSS	26.2	4.331	3.3779	0.6378	10.20
			NREL SOMS @ 1054W/m^2	27.7	4.323	3.5132	0.6438	10.10
566566L	Initial	907.1	United Solar Spire	25	4.57	3.51	0.675	11.9
		905.1	NREL Spire	25.4	4.528	3.3100	0.6769	11.21
			NREL LACSS	27.2	4.488	3.3491	0.6873	11.40
			NREL SOMS @ 988W/m^2	33.9	4.366	3.346	0.6836	11.20
	Stable		NREL Spire	25.1	4.418	3.2996	0.6537	10.53
			NREL LACSS	26.5	4.353	3.2854	0.6598	10.40
			NREL SOMS @ 964W/m^2	28.4	4.327	3.4778	0.6520	10.50
567577L	Initial	918.0	United Solar Spire	25	4.60	3.57	0.678	12.1
		918.0	NREL Spire	25.4	4.535	3.2864	0.6837	11.10
			NREL LACSS	27.0	4.490	3.4215	0.6772	11.30
			NREL SOMS @ 970W/m^2	32.1	4.393	3.2424	0.6840	10.90
	Stable		NREL Spire	25.4	4.408	3.2551	0.6462	10.10
			NREL LACSS	27.9	4.302	3.3228	0.6513	10.10
			NREL SOMS @ 964W/m^2	28.6	4.322	3.5253	0.6413	10.10
563946L	Initial	919.3	United Solar Spire	25	4.58	3.54	0.700	12.3
		919.0	Sandia National	25	4.49	3.5	0.684	11.7
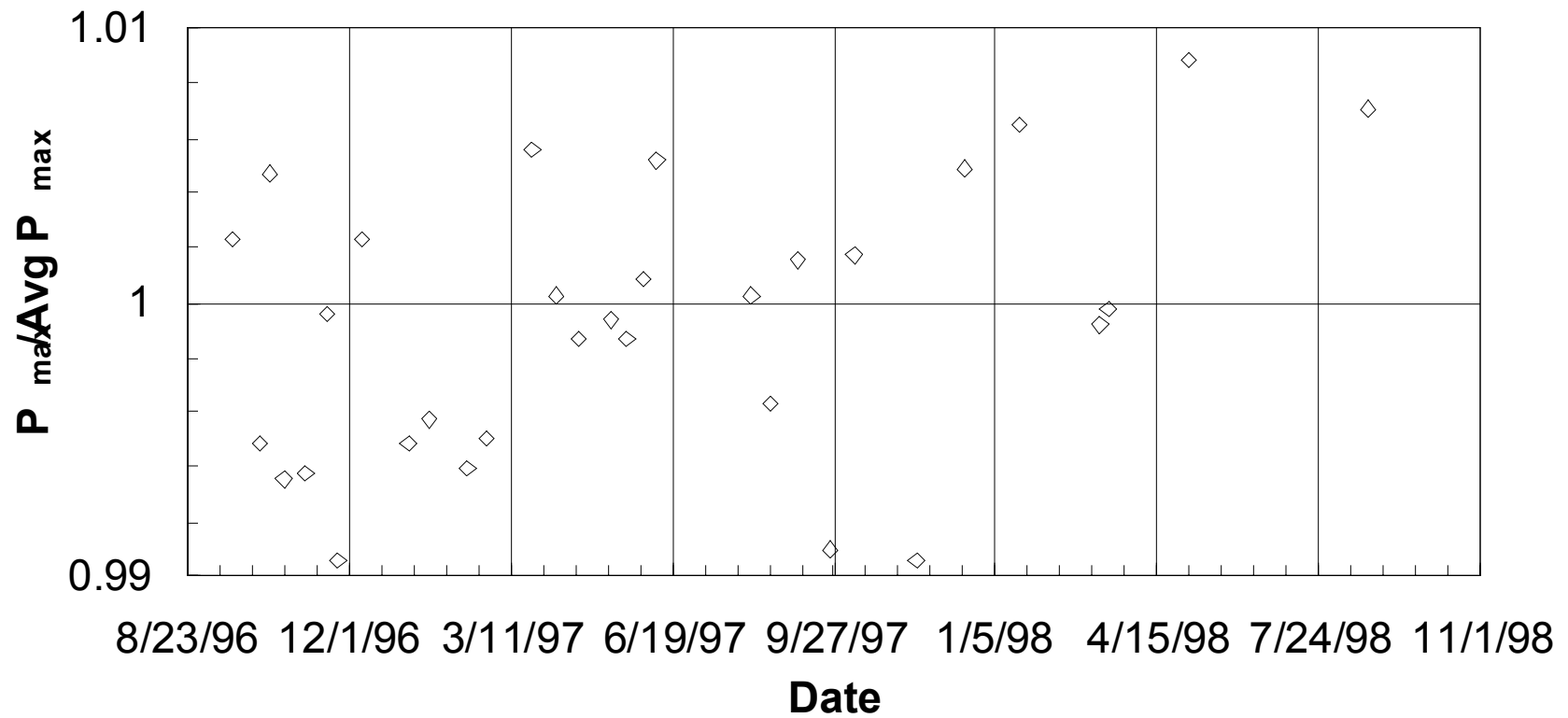
Figure 27. Normalized p_max of a c-Si module measured under United Solar Spire as a function of time.

Table 19. Earlier and Recent Spire Measurements at United Solar and NREL of Old and New Modules.

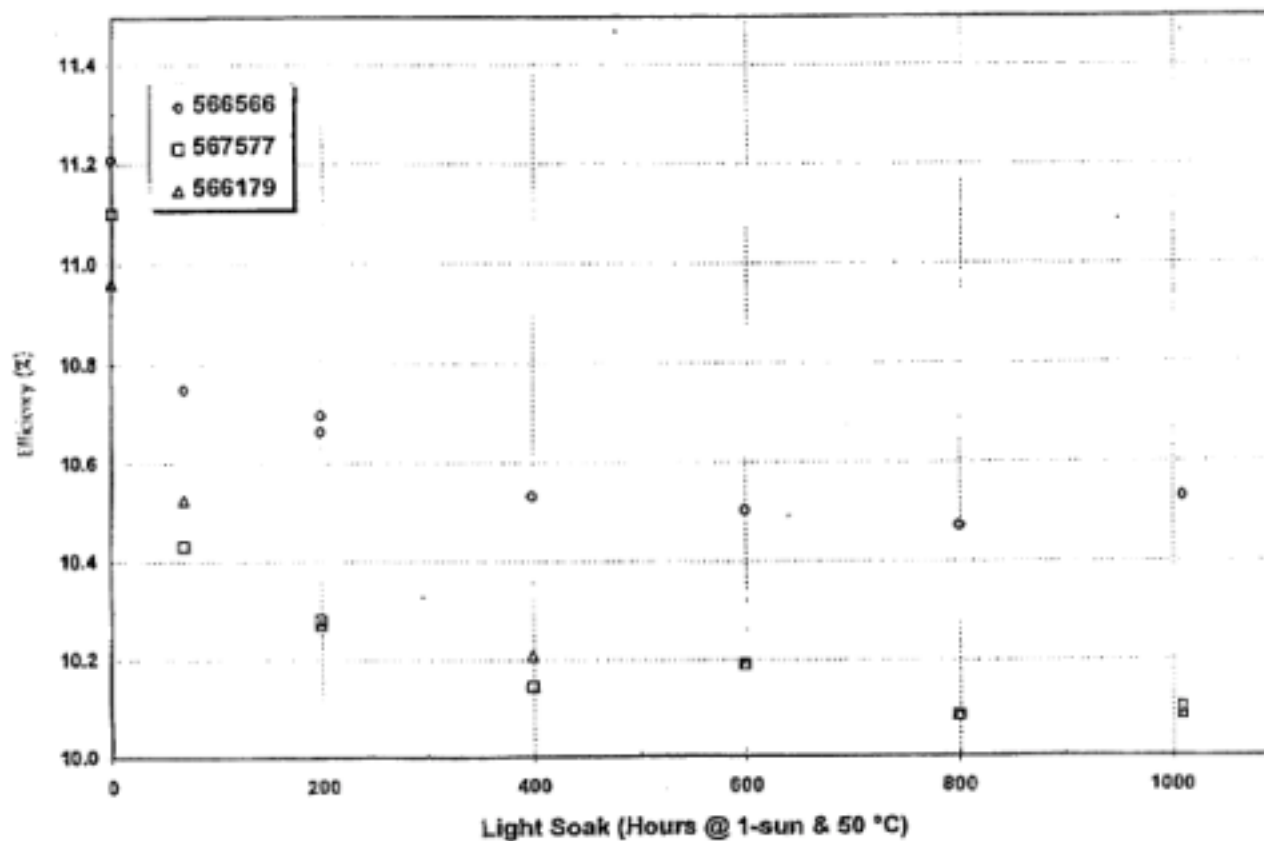| Module	Type	Area (cm^2)	Lab.	Date	V_{oc} (V)	I_{sc} (A)	Diff.(%)	FF	Diff.(%)	V_{max} (V)	I_{max} (A)	P_{max} (W)	Efficiency (%)	Diff.(%)
2B2469F	Old R&D	901.2	USSC	Nov, 93	2.37	6.25		0.654		1.81	5.36	9.68	10.7	
				Sept, 98	2.42	6.39	2.2	0.627	-4.1	1.84	5.27	9.72	10.8	0.4
2B2438F	Old R&D	900.0	USSC	Nov, 93	2.36	5.97		0.689		1.92	5.05	9.70	10.8	
				Sept, 98	2.41	6.26	4.9	0.654	-5.1	1.88	5.25	9.87	11.0	1.8
2B2431F	Old R&D	901.7	USSC	Dec, 93	2.38	6.04		0.680		1.95	5.01	9.75	10.8	
				Sept, 98	2.45	6.24	3.3	0.662	-2.6	1.95	5.19	10.11	11.2	3.7
2B2452F	Old R&D	902.1	USSC	Nov, 93	2.35	6.11	-7.0	0.697	3.3	1.96	5.1	10.00	11.1	-5.5
		905.9	NREL	Dec, 93	2.400	6.568		0.675		1.917	5.553	10.64	11.75	
2B2465F	Old R&D	901.2	USSC	Nov, 93	2.37	6.28	-7.1	0.676	3.7	1.9	5.28	10.06	11.2	-4.2
		902.9	NREL	Dec, 93	2.395	6.757		0.652		1.874	5.631	10.55	11.69	

Figure 28. United Solar modules 566566, 567577, 566179: Spire efficiency measurements.

Summary of Large-area Results

A summary of all the large-area stable results for the component cells, triple-junction devices, and triple-junction modules are given in Table 20. The corresponding milestones for Phase I of the program are also tabulated. Note that for the triple-junction module, the NREL data measured using both the Spire and outdoor SOMS methods is given. The data show that all the milestones have been achieved.

Table 20. Summary of all stable results and corresponding Phase I milestones.

Sample #	Measurement Spectrum	Total area (cm^2)	V_{OC} (V)	FF	J_{SC} (mA/cm^2)	Efficiency (%)	
						Stable	Initial
Top cell on stainless steel							
2B5735	AM1.5	0.268	0.939	0.695	8.8	5.4	5.9
Phase I milestone	AM1.5	~1				5.0	
Middle cell on stainless steel (mW/cm^2)							
2B5905	$\lambda > 530nm$	0.268	0.689	0.589	9.4	3.6	4.4
Phase I milestone	$\lambda > 530nm$	~1				3.1	
Bottom cell on back reflector (mW/cm^2)							
	$\lambda > 630nm$	0.268	0.574	0.548	10.87	3.2	3.8
Phase I milestone	$\lambda > 630nm$	~1				3.1	
Triple-junction cell on back reflector							
2B5616	AM1.5	0.268	2.201	0.666	8.51	11.6	12.5
Phase I milestone	AM1.5	~1				11.2	
Triple-junction module on back reflector							
2B566566L	AM1.5	918				10.5*	
Phase I milestone	AM1.5	~900				10.5	

    *   NREL measurements

Large Area Prototype Modules

We have investigated methods and processes for fabricating large-area flexible modules of two different sizes. One size has a nominal outside dimension of 216"x29.6", and the other size is 216"x15.5". The material and processes used for these prototype modules are compatible with United Solar's current production line. The larger size of the prototype module, however, is two times the largest standard rigid product. The motivation for investigating the methods of fabrication these 18" long flexible modules is to evaluate and qualify each step of the manufacturing process. We have successfully completed qualifying each step in the process and one prototype module from each size was delivered to NREL. The 216"x 15.5" module was measured by NREL on October 20, 1998 to produce 155.5W under outdoor conditions at 1025 W/m^2 irradiance. The module temperature was 39^0C-45^0C. The 216"x.29.6" module was measured by NREL on December 3, 1998 to produce 317.8 W under outdoor conditions at 1044 W/m^2 irradiance The module temperature was 34^0C-39^0C. Assuming a typical degradation of 15%, the modules should stabilize to ~130 W and 260 W, respectively, higher than the 125 W and 250 W goals.

IEEE Std 1262-1995 Qualification of Modules

United Solar has carried out a detailed and systematic qualification of its commercial products. We have sent out many of these products to the Department of Electronics and Computer Technology at the Arizona State University for lEEE 1262 and IEC 1646 qualification testing. All our products pass the qualification tests. Relevant pages from the test report document are reproduced in the following pages. The R&D modules fabricated for the NREL program have been fabricated using the same materials and processes used in the production line. By the principle of similarity, the R&D modules therefore pass the same tests.

IEEE 1262 AND IEC 1646 TESTS CONDUCTED

All tests listed below were performed at the Photovoltaic Testing Laboratory with the exception of the Humidity-Freeze test and the Damp Heat tests. These tests were performed in a PTL-maintained environmental chamber located at Arizona State University Main campus in Tempe, Arizona. Refer to the flowchart given in Figure 1 for the placement of the following tests in the combined IEEE 1262 and IEC 1646 qualification test sequence:

	IEEE1262/IEC1646 Test or Procedure	Sample(s)	Module Number
1.	Visual Inspection	14 modules	0068, 0070, 0075, 0082, 0083, 0085, 0089, 0090, 0093, 0094, 0096, 0099, 0103, 0105
2.	Electrical Performance	14 modules	0068, 0070, 0075, 0082, 0083, 0085, 0089, 0090, 0093, 0094, 0096, 0099, 0103, 0105
3.	Ground Continuity	14 modules	0068, 0070, 0075, 0082, 0083, 0085, 0089, 0090, 0093, 0094, 0096, 0099, 0103, 0105
4.	Dry Electrical Isolation	14 modules	0068, 0070, 0075, 0082, 0083, 0085, 0089, 0090, 0093, 0094, 0096, 0099, 0103, 0105
5.	Wet Insulation Resistance	14 modules	0068, 0070, 0075, 0082, 0083, 0085, 0089, 0090, 0093, 0094, 0096, 0099, 0103, 0105
6.	Control Module	2 module	0099, 0105
7.	Wet Electrical Isolation	11 modules	0068, 0070, 0075, 0082, 0083, 0085, 0089, 0090, 0093, 0094, 0103
8.	200 Thermal Cycle	2 modules	0070, 0103
9.	Ultraviolet Exposure	2 modules	0075, 0082
10.	50 Thermal Cycle	2 modules	0075, 0082
11.	10 Humidity Freeze Cycle	2 modules	0075, 0082
12.	Termination Robustness	1 module	0075
13.	Twist	0 module[1]	waived
14.	Dynamic Mechanical Load	0 module[2]	waived
15.	Surface Cut Susceptibility	4 modules	0070, 0075, 0082, 0103
16.	Damp Heat	2 modules	0068, 0096
17.	Hail Impact	1 module	0068
18.	Static Mechanical Load	1 modules[3]	0075
19.	Outdoor Exposure	2 modules	0089, 0090
20.	Non-intrusive Hot Spot Endurance	1 module	0089
21.	Non-intrusive Bypass Diode Therm.	1 module	0068
22.	Temperature Coeff. Determination	14 modules[4]	0068, 0070, 0075, 0082, 0083, 0085, 0089, 0090, 0093, 0094, 0096, 0099, 0103, 0105
23.	NOCT Measurement	1 module	0090
24.	NOCT Performance	1 module	0090
25.	Low Irradiance Performance	1 modules	0090
26.	Intrusive Hot Spot Endurance	NA	
27.	Intrusive Bypass Diode Thermal	NA	

The combined qualification test program was completed on September 1, 1998.

---

[1] The twist test was waived because of the module's inherent flexibility.

[2] The dynamic load test was waived because it was inconsistent with the SSR-64's intended application.

[3] Only the positive portion of the static load test was performed. The negative static load test was waived because it was inconsistent with the SSR-64's intended application.

[4] Note that the PTL measures and reports a set of average effective temperature coefficients for all modules used in the test program even though only one module is required by the test standards.

10/08/98 7:43 PM

D:\USSC\USS-8001\Report\8100101.doc

Figure 1. Combined IEEE 1262 and IEC 1215 and IEC 1646 qualification test sequence.
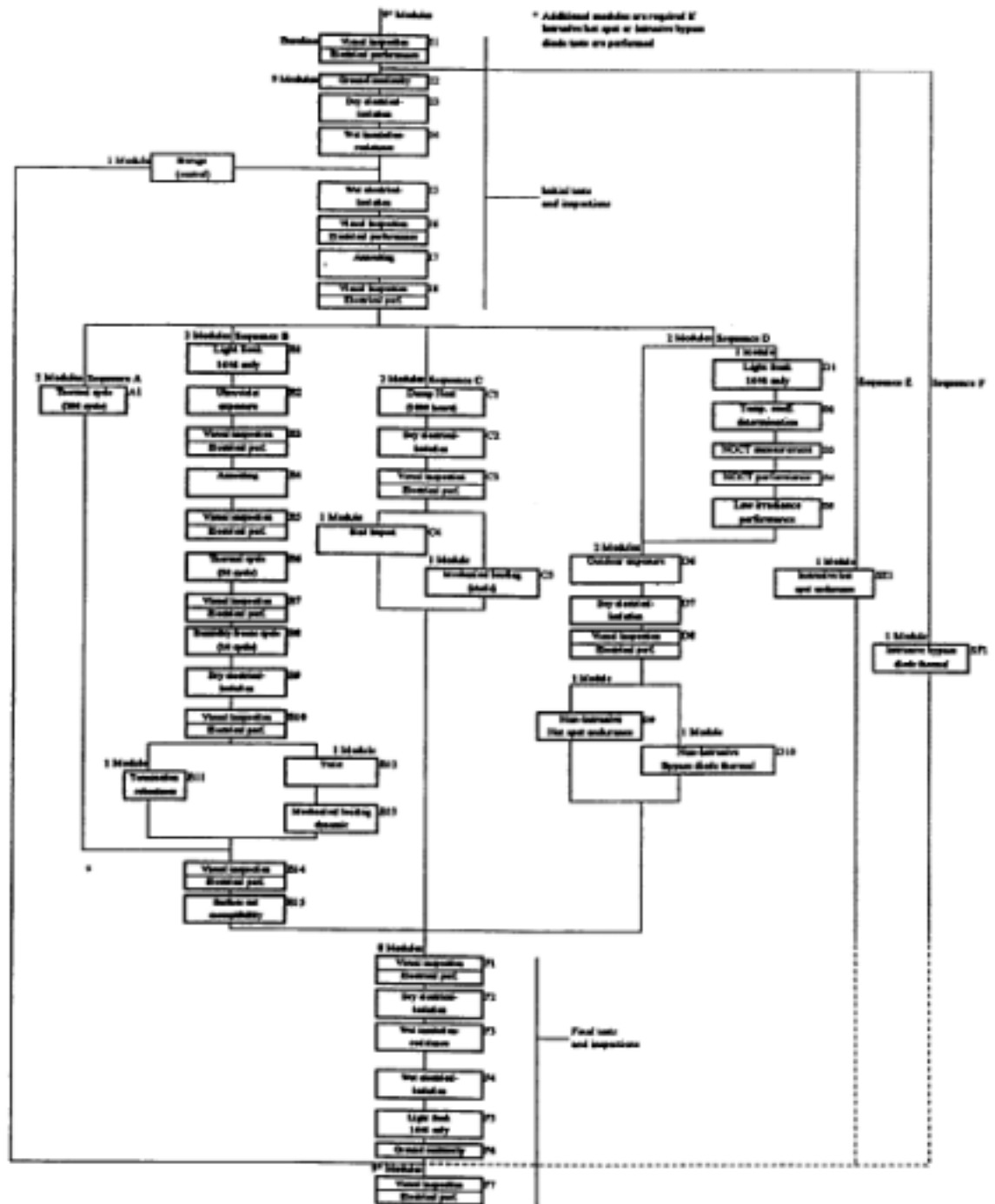
EQUIPMENT USED

The PTL uses equipment calibrated to standards that are traceable to the National Institute of Standards and Technology (NIST) or to standards that have been derived from values of natural physical constants. Detailed laboratory equipment information, including calibration dates and the specific instruments used for each test, is available upon request.

TEST PROCEDURES

Appendix 1 describes how the PTL combines the requirements of IEEE 1262, IEC 1215 and IEC 1646 so that one test program can result in multiple model qualifications.

TEST RESULTS

IEEE 1262 and IEC 1646 qualification testing is a long process and modules that qualify should be reliable and durable for many years. In total, a module must pass fifty to fifty four tests (Sequences E and F are optional and light soaking is required only for thin-film modules) and up to five additional procedures before becoming qualified. All of this testing results in a plethora of data with some more cogent than others. As a result, this part of the report is devoted to the presentation of module testing results in as concise a manner as is possible. Some minor information has, therefore, been omitted for brevity. For example:

1. Visual inspection (per ASTM E 1799-96) requires that the PTL fill-out a 46 point inspection form as often as 9 times for a particular module. Rather than provide all of this information to the reader, we have reported the results as pass/fail.
2. Ground path continuity - only the largest ground path resistance is reported.
3. Electrical isolation tests and insulation resistance tests (wet and dry) - only the largest leakage currents and the smallest insulation resistances are reported.
4. Other tests - only significant results are reported.

The PTL will supply all measured testing data upon request. Please specify those tests or procedures where comprehensive data is required.

Test results are presented in two tables. Table 1 details the dates and significant findings of all tests and Table 2 focuses on the electrical performance for each module as it progressed through the test sequences. Note that the electrical performance data has been translated from actual test conditions to Standard Test Conditions (described below).

General Results

The following table indicates the test dates and significant findings for project USS-8001. A hyphen "-" between dates indicates that testing ran through the two dates given. A comma "," separating dates indicates that the test was performed on different dates for different modules. The first column, Seq., refers to the alphanumeric **Sequence** titles given in Figure 1. Allowables for each test, where relevant, are given parenthetically. Please note that some allowables are based on the aperture area of the module and so the value may appear unusual (i.e., a 44.4 MΩ minimum wet insulation resistance requirement). Refer to Appendix 1 for a complete description of the allowable requirements for the combined qualification test program.

Table 1. Results of Combined Qualification Testing

Combined Qualification Testing IEEE 1262, IEC 1215, IEC 1646, PMC		Test Dates	Findings
Seq.	Test		
I1	Baseline visual inspection	3/18/98, 4/13/98	Pass
I1	Electrical performance (I-V)	3/19/98, 4/13/98	Pass
I2	Ground continuity	3/19/98, 4/14/98	Pass: max. measured resistance=0.0155Ω (max. allowable resistance≤0.10Ω)
I3	Dry Electrical isolation (Dry hi-pot)	3/19/98, 4/14/98	Pass: max. leakage current=0.8 μA (max. allowable leakage current=111 μA) Pass: min. insulation R=2500 MΩ (min. allowable R=50 MΩ)
I4	Wet insulation resistance	3/25/98, 4/17/98	Pass: min. insulation R=555 MΩ (min. allowable R=44.4 MΩ)
I5	Wet Electrical isolation (Wet hi-pot)	3/25/98, 4/17/98	Pass: max. leakage current=4.7μA (max. allowable leakage current=111 μA)
I6	Intermediate visual inspection	3/23/98, 4/17/98	Pass
I6	Electrical performance (I-V)	3/24/98, 4/17/98	Pass
I7	Annealing		waived
I8	Intermediate visual inspection		waived
I8	Electrical performance (I-V)		waived
A1	Thermal cycle (TC200, IEEE)	4/21/98 – 6/13/98	Pass
B1	Light Soak	4/6/98 – 4/29/98	Pass
B2	UV conditioning (15 kWh/m²)	5/11/98 – 6/3/98	Pass: test dosage = 15.29 kWh/m² (required dosage = 15.0 kWh/m²)
B3	Intermediate visual inspection	6/3/98	Pass
B3	Electrical performance (I-V)	6/3/98	Pass
B4	Annealing		waived
B5	Intermediate visual inspection		waived
B5	Electrical performance (I-V)		waived
B6	Thermal cycle (TC50, IEEE)	6/598 – 6/17/98	Pass
B7	Intermediate visual inspection	6/18/98	Pass
B7	Electrical performance (I-V)	6/19/98	Pass
B8	Humidity freeze cycle (HF10)	6/19/98 – 6/30/98	Pass
B9	Dry Electrical isolation (Dry hi-pot)	6/30/98	Pass: max. leakage current=0.6 μA (max. allowable leakage current=111 μA) Pass: min. insulation R=1667 MΩ (min. allowable R=50 MΩ)
B10	Intermediate visual inspection	7/1/98	Pass
B10	Electrical performance (I-V)		See "Additional Information" below
B11	Robustness of terminations	7/13/98	Pass
B12	Twist		waived
B13	Dynamic loading (10,000 cycle)		waived
B14	Intermediate visual inspection	6/13/98, 7/8/98	Pass
B14	Electrical performance (I-V)	6/16/98, 7/9/98	Pass
B15	Surface cut susceptibility	6/23/98, 7/9/98, 7/13/98	Pass
C1	Damp heat (IEEE)	4/9/98 – 5/21/98	Pass

Table 1. Cont.

Combined Qualification Testing IEEE 1262, IEC 1215, IEC 1646, PMC		Test Dates	Findings
Seq.	Test		
C2	Dry Electrical isolation (Dry hi-pot)	5/21/98	Pass: max. leakage current=8.0 µA (max. allowable leakage current=111 µA) Pass: min. insulation R=318.5 MΩ (min. allowable R=50 MΩ)
C3	Intermediate visual inspection	5/26/98	Pass
C3	Electrical performance (I-V)	5/21/98	Pass
C4	Hail impact	6/4/98	Pass: 11 shots, 25.4 mm ice ball, 22.85 m/s (Required: ≥ 10 shots of 25.4 mm ice balls traveling at 23.2 ± 5% m/s)
C5	Static loading	9/1/98	Pass
D1	Light soak	4/15/98 – 5/2/98	Pass
D2	Measurement of α and β	3/18/98, 4/13/98	[1] below
D3	Measurement of NOCT	5/18/98 – 5/27/98	44.4°C
D4	Performance at NOCT	5/27/98	[2] below
D5	Perform. at Low Irradiance	6/8/98	[3] below
D6	Outdoor exposure (60 kWh/m²)	4/22/98 – 5/5/98, 6/11/98 – 6/22/98	Pass
D7	Dry Electrical isolation (Dry hi-pot)	6/23/98	Pass: max. leakage current=0.2 µA (max. allowable leakage current=111 µA) Pass: min. insulation R=5000 MΩ (min. allowable R=50 MΩ)
D8	Intermediate visual inspection	5/13/98, 6/23/98	Pass
D8	Electrical performance (I-V)	5/11/98, 6/22/98	Pass
D9	Hot spot endurance (non-intrusive)	6/2/98	Pass
D10	Bypass diode thermal (non-intrusive)	7/23/98	Pass: 92°C @ Isc and 75°C mod. Temp.
E1	Hot spot endurance (intrusive)		NA
SF1	Bypass diode thermal (intrusive)		NA
F1	Intermediate visual inspection	6/24/98	Pass
F1	Electrical performance (I-V)	6/26/98, 7/2/98, 7/9/98	Pass
F2	Dry Electrical isolation (Dry hi-pot)	6/8/98, 6/10/98, 7/1/98, 7/14/98	Pass: max. leakage current=3.9 µA (max. allowable leakage current=111 µA) Pass: min. insulation R=333 MΩ (min. allowable R=50 MΩ)
F3	Wet insulation resistance	6/10/98, 7/2/98, 7/14/98, 7/15/98	Pass: min. insulation R=143 MΩ (min. allowable R=44.4 MΩ)
F4	Wet Electrical isolation (Wet hi-pot)	6/10/98, 7/2/98, 7/14/98, 7/15/98	Pass: max. leakage current=16 µA (max. allowable leakage current=111 µA)
F5	Light soak	6/11/98–7/10/98, 7/2/98 – 8/21/98	Pass
F6	Ground continuity	7/14/98, 7/22/98, 8/31/98	Pass: max. measured resistance=0.052Ω (max. allowable resistance≤0.10Ω)
F7	Final visual inspection	8/31/98	Pass
F7	Electrical performance (I-V)	7/10/98, 8/21/98	Pass

Section 5

Future Directions

During Phase I of this program, we have witnessed the tremendous interest that has been generated in the amorphous silicon alloy photovoltaic field on materials and solar cells prepared near the threshold of microcrystallinity. World record solar cells and modules have been made in our laboratory using deposition conditions near the threshold. We plan to continue research on near-threshold materials and solar cells, especially on a-SiGe alloys and cells.

Materials and solar cells made by MVHF at high rates show promise, especially for a-Si alloys and top cells. Low bandgap a-SiGe alloys and bottom cells, however, need to be improved significantly in order to achieve high efficiency multijunction devices. Fundamental material quality will be investigated and multijunction devices evaluated.

We have made new world record modules of 10.5% stable aperture-area efficiency during Phase I. We plan to continue our efforts in achieving higher efficiencies by systematic studies of loss mechanisms and improve uniformity even further. Any insight toward achieving higher quality materials by studying near-threshold a-Si and a-SiGe alloys will certainly enhance our understanding and improve device and module efficiencies.

References

Chatham, H.; Bhat, P. K. (1989). *Mater. Res. Soc. Symp. Proc.*; Vol. 149, p. 447.

Gallagher, A. (1999). Private communication.

Guha, S.; Narasimhan, K.L.; Pietruszko, S.M. (1981). *J. Appl. Phys.*; Vol. 52, p. 859.

Guha, S.; Yang, J.; Pawlikiewicz, A.; Glatfelter, T.; Ross, R.; Ovshinsky, S.R. (1989). *Appl. Phys. Lett.*; Vol. 54, p. 2330.

Guha, S.; Yang, J.; Jones, S.J.; Chen, Y.; Williamson, D.L. (1992). *Appl. Phys. Lett.*; Vol. 61, p. 1444.

Guha, S.; Xu, X.; Yang, J.; Banerjee, A. (1995). *Appl. Phys. Lett.*; Vol. 66, p. 595.

Guha, S.; Yang, J.; Banerjee, A.; Glatfelter, T.; Vendura, G.J., Jr.; Garcia, A.; Kruer, M. (1998). *2nd World Conf. and Exhibition on Photovoltaic Solar Energy Conversion Proc., Vienna, Austria, July 6-10, 1998*; p. 3609.

Guha, S.; Yang, J.; Williamson, D.L.; Lubianiker, Y.; Cohen, J.D.; Mahan, A.H. (1999). *Appl. Phys. Lett.*; Vol. 74, p. 1860.

Harmers, E.A.G; Bezermer, J.; Meiling, H.; van Spark, W.G.J.H.M.; van der Weg, W.F. (1997). *Mater. Res. Soc. Symp. Proc.*; Vol. 467, p. 603.

Jiang, L.; Wang, Q.; Schiff, E.A.; Guha, S.; Yang, J.; Deng, X. (1996). *Appl. Phys. Lett.*; Vol. 69, p. 3063.

Jones, S.J.; Chen, Y.; Williamson, D.L.; Xu, X.; Yang, J.; Guha, S. (1993). *Mater. Res. Soc. Symp. Proc.*; Vol. 297, p. 815.

Kamei, T.; Stradius, P.; Matsuda, A. (1999). *Appl. Phys. Lett.*; Vol. 74, p. 1707.

Koh, J.H.; Lee, Y.; Fujiwara, H.; Wronski, C.R.; Collins, R.W. (1998). *Appl. Phys. Lett.*; Vol. 73, p. 1526.

Mahan, A.H.; Yang, J.; Guha, S. (1999). *Mater. Res. Soc. Symp. Proc.* (to be published).

Platz, R.; Wagner, S.; Hof, C.; Shah, A.; Wieder, S.; Rech, B. (1988). *J. Appl. Phys.*; Vol. 84, p. 3949.

Rannels, J. (1998). *2nd World Conf. and Exhibition on Photovoltaic Solar Energy Conversion Proc., Vienna, Austria, July 6-10, 1998*; p. LXXXVII.

Shah, A.; Dutta, J.; Wyrsch, N.; Prasad, K.; Curtins, H.; Finger, F.; Howling, A.; Hollenstein, Ch. (1989). *Mater. Res. Soc. Symp. Proc.*; Vol. 258, p. 15.

Shah, A.; Meier, J.; Torres, P.; Kroll, U.; Fischer, D.; Beck, N.; Wyrsch, N.; Keppner, H. (1997). *Conference Record of the Twenty Sixth IEEE Photovoltaic Specialists Conference-1997*; p. 569.

Shima, J.; Terakawa, A.; Isomura, M.; Tanaka, M.; Kiyama, S.; Tsuda, S. (1997). *Appl. Phys. Lett.*; Vol. 71, p. 84.

Staebler, D.L.; Wronski, C.R. (1977). *Appl. Phys. Lett.*; Vol. 31, p. 292.

Sugiyama, S.; Yang, J.; Guha, S. (1997). *Appl. Phys. Lett.*; Vol. 70, p. 378.

Tsu, D.V.; Chao, B.S.; Ovshinsky, S.R.; Guha, S.; Yang, J. (1997). *Appl. Phys. Lett.;* Vol. 71, p. 1317.

van Spark, W.G.J.H.M.; Bezermer, J.; van der Heijden, R.; van der Weg, W.F. (1996). *Mater. Res. Soc. Symp. Proc.*; Vol. 420, p. 21.

von Roedern, B.; Zweibel, K.; Schiff, E.; Cohen, J.D.; Wagner, S.; Hegedus, S.S.; Peterson, T. (1997). *AIP Conference Proceedings*; Vol. 394, p. 3.

Williamson, D.L. (1995). *Mater. Res. Soc. Symp. Proc.*; Vol. 377, p. 251.

Williamson, D.L. (1999). *Mater. Res. Soc. Symp. Proc.* (to be published).

Xu, X.; Yang, J.; Guha, S. (1996). *J. Non-Crys. Solids*; Vol. 198-200, p. 96.

Yan, B.; Yang, J.; Guha, S.; Gallagher, A. (1999). *Mater. Res. Soc. Symp. Proc.* (to be published).

Yang, J.; Xu, X.; Guha, S. (1994). *Mater. Res. Soc. Symp. Proc.*; Vol. 336, p. 687.

Yang, J.; Banerjee, A.; Glatfelter, T.; Hoffman, K.; Xu, X.; Guha, S. (1994). *1st World Conf. on Photovoltaic Energy Conversion, Waikoloa, Hawaii, Dec. 5-9, 1994*; p. 380.

Yang, J.; Banerjee, A.; Guha, S. (1997). *Appl. Phys. Lett.*; Vol. 70, p. 2975.

Yang, J.; Sugiyama, S.; Guha, S., (1998). *Mater. Res. Soc. Symp. Proc.*; Vol. 507, p, 157.

Yang, J.; Guha, S. (1999). *Mater. Res. Soc. Symp. Proc.* (to be published).

Yang L.; Chen, L. (1994). *Mater. Res. Soc. Symp. Proc.*; Vol. 336, p. 669.

REPORT DOCUMENTATION PAGE

1. AGENCY USE ONLY (Leave blank)	2. REPORT DATE July 1999	3. REPORT TYPE AND DATES COVERED Annual Technical Progress Report, 6 March 1998 – 5 March 1999

4. TITLE AND SUBTITLE

High-Efficiency Triple-Junction Amorphous Silicon Alloy Photovoltaic Technology; Annual Technical Progress Report, 6 March 1998 – 5 March 1999

6. AUTHOR(S)

S. Guha

5. FUNDING NUMBERS

C: ZAK-8-17619-09
TA: PV905001

7. PERFORMING ORGANIZATION NAME(S) AND ADDRESS(ES)

United Solar Systems Corp.
1100 West Maple Road
Troy, MI 48084

8. PERFORMING ORGANIZATION REPORT NUMBER

9. SPONSORING/MONITORING AGENCY NAME(S) AND ADDRESS(ES)

National Renewable Energy Laboratory
1617 Cole Blvd.
Golden, CO 80401-3393

10. SPONSORING/MONITORING AGENCY REPORT NUMBER

SR-520-26648

11. SUPPLEMENTARY NOTES

NREL Technical Monitor: K. Zweibel

12a. DISTRIBUTION/AVAILABILITY STATEMENT

National Technical Information Service
U.S. Department of Commerce
5285 Port Royal Road
Springfield, VA 22161

12b. DISTRIBUTION CODE

13. ABSTRACT *(Maximum 200 words)*

This report describes the research performed during Phase I of this three-phase, three-year program. The research program is intended to expand, enhance, and accelerate knowledge and capabilities for developing high-performance, two-terminal multijunction amorphous silicon (a-Si) alloy cells and modules with low manufacturing cost and high reliability. To improve efficiency, United Solar uses a spectral-splitting, triple-junction cell structure. In this configuration, the top cell uses an amorphous silicon alloy of ~1.8 eV bandgap to absorb the blue photons. The middle cell uses an amorphous silicon germanium alloy (~20% germanium) of ~1.6 eV bandgap to capture the green photons. The bottom cell has ~40% germanium to reduce the bandgap to ~1.4 eV to capture the red photons. The cells are deposited on stainless steel with a predeposited silver/zinc oxide back reflector to facilitate light trapping. A thin layer of antireflection coating is applied to the top of the cell to reduce reflection loss. During this year, research activities were carried out in the following four areas: 1) fundamental studies to improve our understanding of materials and devices, 2) small-area cell research to obtain the highest cell efficiency, 3) deposition of small-area cells using a modified very high frequency (MVHF) technique to obtain higher deposition rates, and 4) large-area cell research to obtain the highest module efficiency.

14. SUBJECT TERMS

photovoltaics ; amorphous silicon alloy materials ; high-efficiency cells ; triple-junction cells ; small-area cell research ; large-area module research

15. NUMBER OF PAGES

16. PRICE CODE

17. SECURITY CLASSIFICATION OF REPORT Unclassified	18. SECURITY CLASSIFICATION OF THIS PAGE Unclassified	19. SECURITY CLASSIFICATION OF ABSTRACT Unclassified	20. LIMITATION OF ABSTRACT UL